

Cooperation and competition of basepairing and electrostatic interactions in mixtures of DNA nanostars and polylysine

Gabrielle R. Abraham,^{1,*} Tianhao Li,² Anna Nguyen,³ William M. Jacobs,^{2,†} and Omar A. Saleh^{1,3,4,‡}

¹*Physics Department, University of California, Santa Barbara*

²*Chemistry Department, Princeton University*

³*Biomolecular Science and Engineering Program, University of California, Santa Barbara*

⁴*Materials Department, University of California, Santa Barbara*

Phase separation in biomolecular mixtures can result from multiple physical interactions, which may act either complementarily or antagonistically. In the case of protein–nucleic acid mixtures, charge plays a key role but can have contrasting effects on phase behavior. Attractive electrostatic interactions between oppositely charged macromolecules are screened by added salt, reducing the driving force for coacervation. By contrast, base-pairing interactions between nucleic acids are diminished by charge repulsion and thus enhanced by added salt, promoting associative phase separation. To explore this interplay, we combine experiment and theory to map the complex phase behavior of a model solution of poly-L-lysine (PLL) and self-complementary DNA nanostars (NS) as a function of temperature, ionic strength, and macromolecular composition. Despite having opposite salt dependences, we find that electrostatics and base pairing cooperate to stabilize NS-PLL coacervation at high ionic strengths and temperatures, leading to two-phase or three-phase coexistence under various conditions. We further observe a variety of kinetic pathways to phase separation at different salt concentrations, resulting in the formation of nonequilibrium aggregates or droplets whose compositions evolve on long timescales. Finally, we show that the cooperativity between electrostatics and base pairing can be used to create multiphase coacervates that partition various NS species at intermediate salt concentrations. Our results illustrate how the interplay between distinct interaction modes can greatly increase the complexity of the phase behavior relative to systems with a single type of interaction.

I. INTRODUCTION

Solutions of macromolecules in solvent can spontaneously separate into spatially distinct regions that are, respectively, dense and dilute in the macromolecules. Frequently, the dense phase retains liquid-like properties, and the process is termed liquid-liquid phase separation (LLPS). LLPS is driven by net attractive interactions between macromolecules, including those that are mediated by the solvent or cosolutes, such as electrostatic, hydrogen-bonding, or hydrophobic interactions. These interactions can be between molecules of the same species (“homotypic”), between molecules of different species (“heterotypic”), or a combination of the two.

Recently, interest in biomolecular LLPS has surged due to its role in the formation of biomolecular condensates, which provide spatial and temporal organization within living cells. *In vivo* LLPS of proteins and nucleic acids has been implicated in numerous processes, such as transcription and stress response [1–3]. Engineering biomolecular LLPS for technological applications is also of interest, for example to control cellular behavior for synthetic biology purposes [4] or to create multiphase *in vitro* structures that can be used to build complex materials [5] or bioreactors [6].

Predicting and controlling biomolecular LLPS in the multicomponent settings that are biologically and/or technologically relevant remains challenging due to the wide variety of physicochemical interactions that can contribute to both homotypic and heterotypic interactions between various molecules. Numerous studies have analyzed the effects of specific interaction modalities—including interactions between folded protein domains [7], hydrophobic interactions between aromatic residues in prion-like domains in disordered proteins [8], electrostatic interactions in binary mixtures of oppositely charged disordered proteins [9], and base-pairing among RNA oligonucleotides [10]—within controlled, *in vitro* reconstitutions of biomolecular mixtures. Nonetheless, further work is needed to explore the interplay among these various types of interactions, in particular in biomolecular mixtures with both homotypic and heterotypic interactions.

Here, we carry out an experimental and theoretical analysis of LLPS in the presence of both homotypic, base-pairing driven association and heterotypic, electrostatically driven coacervation in a multicomponent biomolecular mixture with well-defined interactions. Our experimental system is based on a model system of DNA nanoparticles termed nanostars (NSs), branched DNA particles that interact through single-stranded sequences (“sticky ends”) [11]. NSs can be designed with sticky ends that are palindromic, allowing homotypic binding with a neighboring NS with an identical sequence and leading to associative LLPS. Previous studies have investigated the effect on LLPS of various NS design param-

* Current address: Physics Department, University of Southern California

† wjacobs@princeton.edu

‡ saleh@ucsb.edu

ters, including sequence-dependent intermolecular interactions [12, 13], particle flexibility [12, 14, 15] and valence [11, 16–18]. In this work, we explore the interplay between homotypic base-pairing and heterotypic interactions due to electrostatic attraction between NSs and poly-L-lysine (PLL), a positively charged polypeptide that can form heterotypic droplets or gels when mixed with single- or double-stranded nucleic acids. Previous studies have shown that the presence and nature of the condensed phase are sensitive to the salt conditions, as well as the structure of the nucleic acid, due to the dominant role of electrostatics in driving phase separation [10, 19–22].

The central aim of this work is to understand how the interplay between electrostatic interactions and base pairing determines the phase behavior of NS+PLL mixtures. In particular, we investigate the effects of charge screening by added salt on these two interaction modalities, which is well-known to strengthen base-pairing interactions but weaken the driving force for electrostatic coacervation. Using fluorescent microscopy, we observe a diversity of liquid- and gel-like phase behaviors of NS+PLL mixtures and, by characterizing each phase’s molecular composition and temperature response, we determine the dominant interaction mode for the phase in a given set of conditions. In parallel, we develop an analytical model of the free energy of the NS+PLL mixture that treats base-pairing and electrostatics on equal footing and thus allows us to predict the phase behavior of the solution. Experiments and theory both reveal rich phase behavior, including transitions between dense phases that are alternatively electrostatically or base pairing-dominated. We further show that these two interaction modalities can either cooperate to stabilize a single dense phase or compete to form distinct dense phases. Our findings indicate that the strengths of NS-NS and NS-PLL interactions are closely tuned in the studied conditions, permitting distinct phase behaviors to appear upon relatively modest environmental changes. Overall, our results demonstrate that rich phase behavior can arise from a simple set of molecular interactions—within a biologically relevant range of solutions conditions—and provide a quantitative understanding of this diversity.

II. RESULTS

A. NS design and NS-only associative phase separation

Experiments were carried out with DNA NSs that were self-assembled from four DNA oligomers by thermal annealing, following prior work [16] (Fig. 1A). Each NS consists of four double-stranded DNA arms that meet at a junction and terminate at the distal end in a single-stranded segment. Each arm either terminates in an overhanging palindromic sticky-end sequence, 5'-CGATCG-3',

that is capable of binding a second identical segment, or a non-palindromic sequence that cannot engage in such homotypic interactions. Fluorescent imaging revealed that solutions of palindromic NSs (pNSs) phase separate at high salt (Fig. 1B and Fig. S1), whereas those with non-palindromic NSs (npNSs) were not found to phase separate under any conditions (Fig. S1). Varying the salt concentration further showed that solutions with 10 μ M pNS do not phase separate at and below 75 mM NaCl (Fig. 1C and Fig. S1). These observations are consistent with associative phase separation driven by the hybridization of pNS sticky ends above a lower critical salt concentration. Decreasing the NaCl concentration reduces the driving force for phase separation, since the attractive base-pairing interactions weaken due to reduced electrostatic screening between the charged sticky ends [23].

B. Complex coacervation of NS and PLL

To investigate the effects of electrostatically driven heterotypic interactions, we mixed npNSs with 100-residue long PLL in a concentration ratio chosen to match the macromolecular charge densities (i.e., 10 μ M npNS and 19.2 μ M PLL, assuming total charges of $-192e$ and $100e$ per molecule, respectively). Both NSs and PLL were labeled with distinct fluorescent dyes to permit identification of the presence and composition of dense phases through fluorescent imaging. We found that npNS+PLL mixtures form gels at low salt, coexisting dilute and liquid-like dense phases at intermediate salt, and a single mixed phase at high salt (Fig. 1A,D,E and Fig. S2). We observed similar behavior in mixtures of PLL and “blunt” NSs, which do not include any single-stranded sticky ends on the NS arms, confirming that the high-salt dissolution of npNS+PLL condensates does not depend on the presence of sticky ends (Fig. S2). These results are consistent with prior nucleic-acid/PLL studies [24], indicating that npNS+PLL dense phases are predominantly stabilized by heterotypic electrostatic attractions. This behavior, commonly referred to as (complex) coacervation, exhibits an upper critical salt concentration, since higher salt concentrations more effectively screen the heterotypic electrostatic attractions. For the same reason, sufficiently low salt concentrations result in less screened electrostatic interactions that are strong enough to oppose relaxation and coarsening of the dense phase [24–27], which is consistent with our observations of kinetically trapped gel structures at 0.25 M NaCl (Fig. S2).

C. Mixed interaction modalities

Having established that the individual homotypic and heterotypic interactions respond oppositely to changes in salt concentration due to the respective lower and upper critical behavior of pNS and npNS+PLL solutions, we next investigated the phase behavior with both

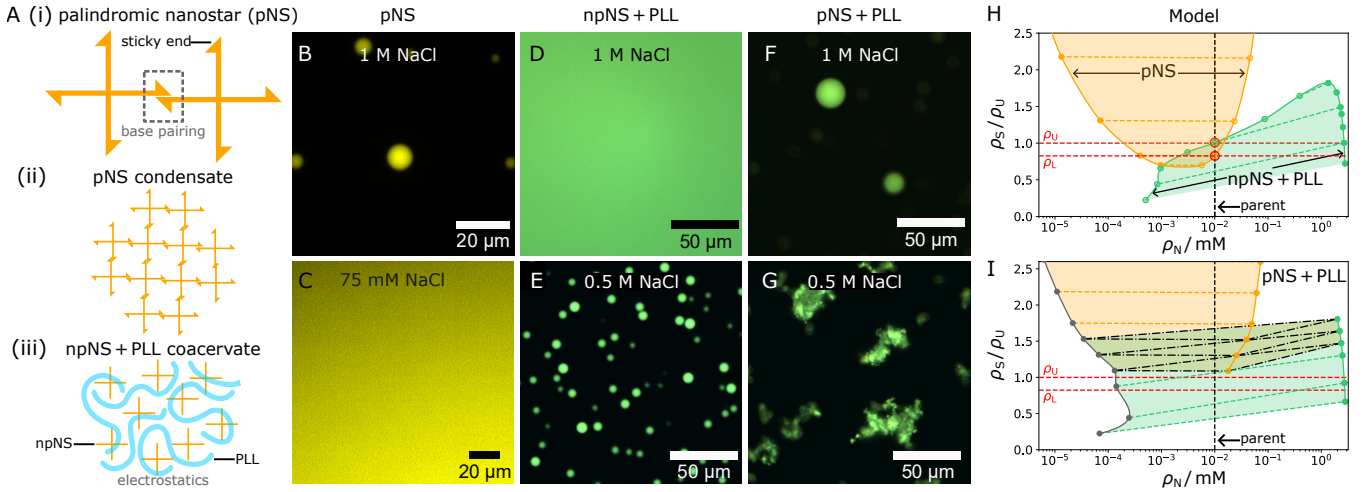


Figure 1. Overview of nanostar (NS) and poly-L-lysine (PLL) phase behavior. (A) Schematics of (i) a four-armed DNA nanostar with palindromic sticky ends (pNS), (ii) associative phase separation driven by sticky-end base pairing, and (iii) coacervation of nonpalindromic nanostars (npNS) with PLL due to electrostatic interactions. (B-G) Fluorescent images of pNS (yellow), npNS (yellow), and/or PLL (cyan) mixtures, performed at $10 \mu\text{M}$ NS and $19.2 \mu\text{M}$ PLL. (B) A pNS solution phase separates at 1 M NaCl , but (C) remains in a single phase at 0.075 M NaCl . (D) A npNS+PLL solution exists as a single phase at 1 M NaCl , but (E) forms spherical, liquid-like droplets at 0.5 M NaCl . (F) By contrast, a pNS+PLL solution phase separates at 1 M NaCl to form droplets, but (G) is arrested in a gel-like aggregate at 0.5 M NaCl . (H) Coexistence regions predicted from our theoretical model for, respectively, pNS and npNS+PLL solutions as a function of NS concentration, ρ_N , and salt concentration, ρ_S . In the npNS+PLL case, the solution is assumed to be macromolecularly charge balanced, so that $\rho_P = (192/100)\rho_N$. Solid curves and points indicate coexistence curves, and dashed lines indicate representative tie lines. The transition salt concentrations ρ_U and ρ_L are defined as the highest and lowest salt concentrations at which phase separation occurs at the experimental parent concentration (vertical line, $\rho_N = 10 \mu\text{M}$) in the npNS+PLL and pNS solutions, respectively. (I) Predicted phase diagram for macromolecularly charge-balanced pNS+PLL mixtures showing both two-phase (green and yellow tie lines) and three-phase (black tie lines) coexistence regions. Note that the tie lines are shown as straight lines for clarity but are in fact curved on these semilog phase diagrams.

types of interactions present. To this end, we created macromolecularly charge-balanced pNS+PLL mixtures ($10 \mu\text{M}$ pNS and $19.2 \mu\text{M}$ PLL) at various salt concentrations. These mixtures exhibited both a low-salt gel phase and liquid-like phase coexistence at higher salt concentrations. Yet compared to npNS+PLL mixtures, the pNS+PLL gel/liquid transition occurs at a higher salt concentration. Moreover, liquid-like droplets persist to higher salt concentrations without evidence of an upper critical salt concentration (Fig. 1F,G) and remain stable over several days, suggesting that the phase-separated solution is close to equilibrium (Fig. S3). These droplets are composed of both pNS and PLL at 1 M NaCl (Fig. 1F), indicating that heterotypic electrostatic interactions contribute to the driving force for phase separation under conditions where electrostatic interactions alone do not lead to coacervation. These observations therefore provide evidence of cooperativity between the heterotypic and homotypic interactions. Specifically, they suggest that the combination of electrostatics and base pairing increases the net strength of the attractive interactions among the NS and PLL molecules. This cooperativity both increases the salt concentration required to avoid gelation and promotes coacervation in the presence of

greater electrostatic screening than is possible in the npNS+PLL mixture.

D. Theoretical model development

To facilitate the interpretation of these observations, we developed a theoretical model to predict the equilibrium phase behavior of NS+PLL mixtures. This model combines a DLVO [28] description of screened electrostatics with a statistical associating fluid theory (SAFT) [29] treatment of sticky-end hybridization, the latter of which has previously been shown to accurately describe NS-only phase behavior [30]. Importantly, these two types of interactions are considered on equal footing within a consistent mean-field framework (see Methods). No other interactions, aside from the entropic effects of excluded volume, are considered for simplicity and interpretability. All model parameters are based on experimental measurements, including the Bjerrum length for screened electrostatics [31] and the temperature and salt-dependence of the sticky-end hybridization free energies [23, 32], as well as the physical properties of the NS and PLL molecules. Details of the model derivation and parametrization are provided in Sections S1–S4.

Applying this model to the pNS-only and npNS+PLL systems produced predictions consistent with the experimental observations and the expected salt dependence of the two separate interaction modalities. In the case of the pNS-only mixture, the model predicts a lower critical salt concentration and a lower transition salt concentration, ρ_L , defined by the intersection of the parent concentration (10 μM pNS) and the binodal (Fig. 1H). By contrast, the npNS+PLL mixture exhibits an upper critical salt concentration and an upper transition salt concentration, ρ_U , at the parent concentration (10 μM npNS, 19.2 μM PLL). In Fig. 1H, we show the binodal for a macromolecularly charge-balanced mixture, in which case the PLL:npNS concentration ratio is the same in the two phases by symmetry. This binodal has the typical shape of DLVO-based theoretical predictions for symmetric polyelectrolyte solutions near the critical point [33], although the predicted dilute-phase concentration at low salt is influenced by the charge and size asymmetry of the npNS and PLL molecules in our model. The values of $\rho_U = 0.23 \text{ M}$ and $\rho_L = 0.19 \text{ M}$ each differ by roughly a factor of three relative to the experimental values of 0.95 M and 0.075 M, respectively; however, the crucial qualitative prediction that $\rho_U > \rho_L$ is consistent with the experimental observations. Throughout the remainder of this article, we normalize our predicted salt concentrations relative to ρ_U when making comparisons with experiments.

When applied to the pNS+PLL system, our model predicts that cooperative phase behavior is due to the comparable strengths of the two interaction modalities at intermediate salt. In particular, for salt concentrations between the upper and lower critical salts of the npNS+PLL and pNS systems, respectively, the model predicts that homotypic pNS interactions substantially reduce the concentration of the dilute phase that coexists with the coacervate (Fig. 1I). This effect implies an increase in the stability of the condensed coacervate phase due to homotypic pNS interactions. As a result, for salt concentrations above approximately ρ_U , the model predicts three-phase coexistence for a range of parent concentrations (Fig. 1I), indicating that coacervate droplets can be in coexistence with both the dilute phase and majority-NS droplets at salt concentrations well above ρ_U at equilibrium. Although experimental observations of all three phases depend on kinetic considerations in practice, as we discuss below, these predictions are consistent with the increased stability of coacervate droplets upon addition of homotypic pNS interactions in Fig. 1F.

E. Temperature dependence of mixed-modality phase behavior

To test the hypothesis that homotypic base pairing is essential for pNS+PLL phase separation at intermediate salt concentrations, we examined the temperature response of pNS+PLL droplets. Homotypic pNS droplets

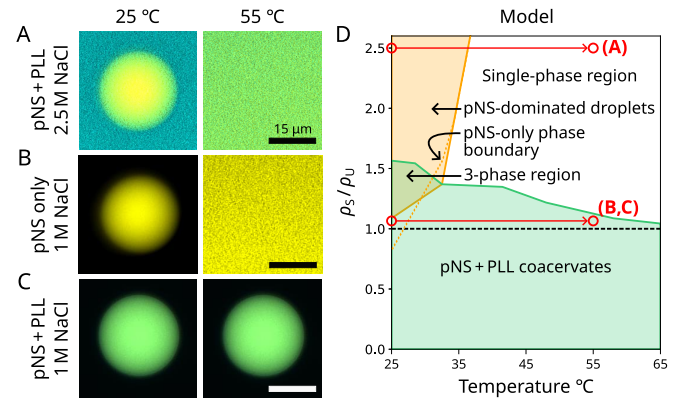


Figure 2. Temperature dependence of single and mixed-modality phase behavior with pNS (yellow) and PLL (cyan). (A) At 2.5 M NaCl, pNS+PLL solutions form NS-dominated liquid-like droplets that are stable at 25 °C but melt at 55 °C. (B) In the absence of PLL, pNS droplets similarly melt at 55 °C at the lower salt concentration of at 1 M NaCl. (C) By contrast, pNS+PLL solutions at 1 M NaCl form liquid-like droplets that are stable at both 25 °C and 55 °C. (D) Predicted pNS+PLL phase diagram as a function of temperature and salt concentration at the parent concentration of 10 μM pNS and 19.2 μM PLL. The phase boundary for a 10 μM pNS-only solution is indicated by a dashed yellow line. The red arrows on this predicted phase diagram correspond to the heating experiments in panels A–C.

(with no PLL present) are known to exhibit upper critical solution temperatures (UCSTs) due to the melting of sticky-end duplexes at elevated temperatures [11, 16]. By contrast, electrostatically stabilized droplets can exhibit more complicated responses to temperature, but frequently exhibit lower critical solution temperatures (LCSTs) due to the dominant entropic contributions to coacervation [34]. We therefore sought to distinguish homotypic and heterotypic interactions via their temperature dependence.

We first verified the expected UCST behavior of homotypically stabilized droplets. At a high salt concentration of 2.5 M NaCl, where increased screening results in negligible electrostatic interactions and enhanced base pairing, droplets in a pNS+PLL mixture melt upon increasing the temperature from 25 °C to 55 °C (Fig. 2A). This behavior is analogous to that of pNS-only solutions, in which we measured the droplet melting temperature at 10 μM pNS and 1 M NaCl to be around 40 °C (Fig. 2B). As anticipated, these observations are consistent with base pairing-driven phase separation.

If pNS+PLL phase separation were dominated by homotypic base pairing at the intermediate salt concentration of 1 M NaCl, then we would expect the pNS+PLL droplets to also dissolve at high temperatures. However, pNS+PLL coacervates are stable for many hours at 55 °C at 1 M NaCl (Fig. 2C). We therefore conclude that because neither electrostatic coacervation nor base pairing alone is sufficient to stabilize droplets under these conditions, phase separation must occur as a result of co-

operative heterotypic and homotypic interactions. This observation supports our hypothesis that phase separation at 25 °C at 1 M NaCl is therefore also a consequence of cooperative electrostatic and basepairing interactions, as predicted by the theoretical model at intermediate salt concentrations.

These observations also agree qualitatively with the temperature dependence predicted by our model. In the model, the temperature dependence of base pairing is introduced through empirical, sequence-dependent sticky-end hybridization free energies [23]. By contrast, the electrostatic contribution to the mean-field free energy is independent of temperature due to the assumption of a temperature-independent Bjerrum length. The resulting temperature and salt-dependent predictions for a solution with a parent concentration of 10 μ M pNS and 19.2 μ M PLL are shown Fig. 2D. At high salt ($\rho_S \gg \rho_U$), the predicted phase boundary for pNS-dominated droplets closely follows the phase boundary for pNS-only solutions at the parent concentration of 10 μ M pNS, since base pairing is the dominant driving force for phase separation in both of these cases. However, in pNS+PLL solutions at intermediate salt ($\rho_S \gtrsim \rho_U$), cooperativity among the two driving forces shifts the phase boundary for coacervation, which occurs at ρ_U in the absence of basepairing interactions by definition, to higher salt concentrations. This predicted increase in the range of conditions at which coacervation can occur is consistent with the observation of pNS+PLL phase separation at intermediate salt concentrations and high temperatures in Fig. 2C (Fig. S4).

F. Nonequilibrium phase behavior revealed by varying macromolecular composition

We then sought to distinguish the contributions of homotypic and heterotypic interactions by varying the macromolecular composition. Electrostatically driven coacervation is typically promoted by macromolecular charge ratios close to unity [24], leading to phase separation in which both the dilute and condensed phases are macromolecularly charge balanced. By contrast, phase separation due to homotypic basepairing interactions requires no neutralizing polycation, and so is likely less sensitive to the macromolecular charge ratio. Therefore, to investigate the role of charge stoichiometry, we explored the phase behavior at 25 °C by holding the pNS concentration fixed at $\rho_N = 10 \mu$ M and tuning the PLL concentration ρ_P to vary the macromolecular charge ratio.

Consistent with these expectations, we found that phase separation is insensitive to the macromolecular charge ratio for salt concentrations at and above 1 M NaCl. At 2.5 M NaCl, pNS-enriched droplets rapidly formed at four charge ratios ranging from 1/8:1 to 1:1 PLL:pNS (Fig. 3A). These droplets were found to exclude PLL shortly after mixing, but then displayed an

increasing enrichment of PLL over several days (Fig. S5). We found that the timescale of PLL penetration is accelerated at higher excess-negative macromolecular charge ratios (14 hours at 1/8:1, versus several days at 1/2:1, versus greater than 3 days at 1:1; Fig. S5) and shorter PLL lengths (1 hour using 20-residue PLL, compared to the 14 hours with 100-residue PLL; Fig. S6). Nonetheless, homotypic interactions appear to provide the dominant initial driving force for phase separation under these conditions, and the partition coefficients remain higher for pNS than for PLL after the long equilibration period (Fig. S7). At a 1 M NaCl, we similarly observed charge ratio-independent phase behavior for macromolecular charge ratios up to 2:1 PLL:pNS (Fig. 3B). Under these conditions, pNSs and PLL quickly colocalize in the dense phase after mixing, and the droplets persist for several days (Fig. S3). These observations are consistent with our prior conclusion that phase separation is driven by cooperative homotypic and heterotypic interactions at 1 M NaCl.

Varying the macromolecular charge ratio has a greater effect at lower salt concentrations, since the heterotypic electrostatic interactions play a more significant role under these conditions. When the polyanion is in sufficient excess (below charge ratios of approximately 1/2:1 PLL:pNS) at salt concentrations below 0.5 M NaCl, we observed coexistence of pNS-enriched droplets with pNS+PLL coacervate gels (Fig. 3C). Such three-phase coexistence is not surprising given that both pNS droplets, in pNS-only solutions, and kinetically arrested coacervate gels, in macromolecularly charge-matched pNS+PLL solutions, can form under these salt conditions. Frequently, we found that the gel forms a layer encasing a larger pNS-enriched droplet, suggesting that the coacervate gels have a lower interfacial tension with the dilute solution and thus preferentially coat the droplets. Moreover, the direct contact between the droplets and coacervate gels under these conditions suggests that complete wetting is thermodynamically favored, which is likely due to the presence of pNS in both phases. By contrast, the phase behavior of mixtures with excess polycation (2:1 PLL:pNS) at 0.5 M is similar to the phase behavior of charge balanced systems (Fig. 3D). The same kinetically arrested morphologies were observed down to a macromolecular charge ratio of 1/2:1 PLL:pNS at 0.25 M NaCl.

Overall, the dependence on the macromolecular charge ratio agrees with the predictions of our theoretical model. For the salt conditions explored (from $\rho_S \lesssim \rho_U$ to $\rho_S \gg \rho_U$), the model predicts equilibrium pNS-enriched droplets at high salt and excess polyanion, NS+PLL coacervates at low salt and excess polycation, and a three-phase region in which both condensed phases coexist at intermediate salt concentrations and macromolecular charge ratios (Fig. 3E; we note that the equilibrium predictions at the 1:1 charge ratio in this figure correspond to the 25 °C phase behavior in Fig. 2D and the ρ_S versus ρ_N projection of the phase diagram in Fig. 1I.)

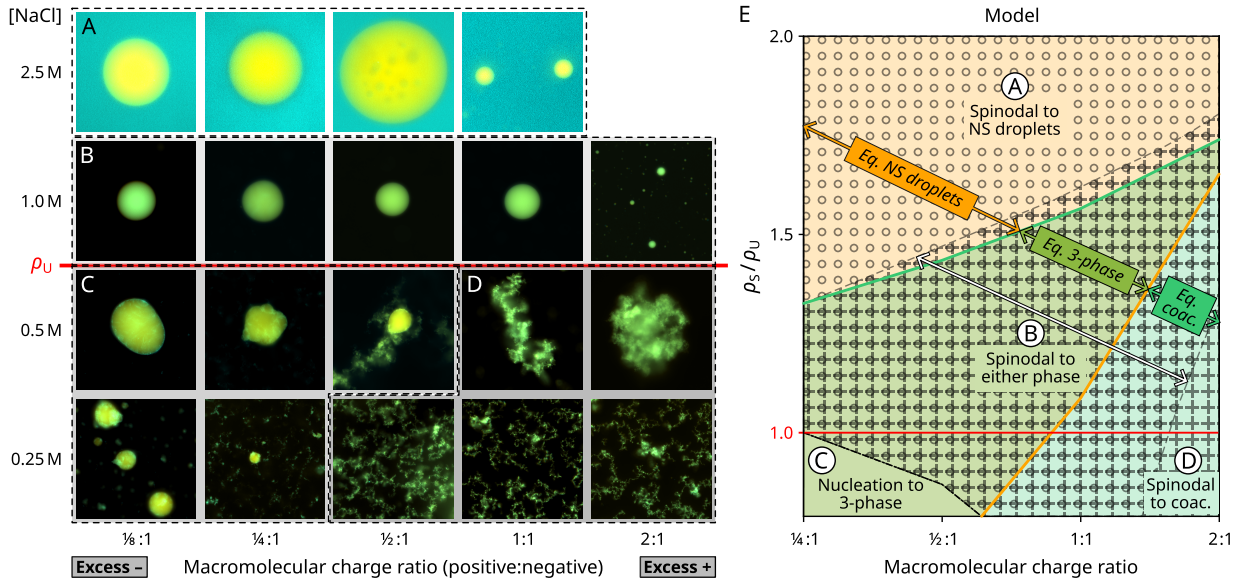


Figure 3. Composition-dependent nonequilibrium phase diagram for pNS (yellow) and PLL (cyan) at constant pNS concentration $\rho_N = 10 \mu\text{M}$ at 25°C . (A) At 2.5 M , pNSs form liquid-like droplets that exclude PLL immediately after mixing. (B) At 1 M NaCl, pNSs and PLL are both enriched in liquid-like droplets. (C) At 0.25 M and 0.5 M NaCl, pNS-enriched liquid-like droplets coexist with, but remain spatially distinct from pNS+PLL gels, when pNS is present in sufficient excess (i.e., excess negative charge). (D) However, at higher PLL concentrations, pNSs and PLL form gels at these salt concentrations. (E) Predicted phase diagram showing both equilibrium and kinetic boundaries for these conditions. At equilibrium, the solution forms either pNS-enriched droplets, pNS+PLL coacervates, or both, depending on the salt concentration ρ_S and the PLL concentration $\rho_P = (192/100) \times (\text{charge ratio}) \times 10 \mu\text{M}$, as indicated by the shaded regions and solid phase boundaries. By contrast, dashed lines delineate conditions where the solution is predicted to undergo spinodal decomposition to NS-enriched droplets or NS+PLL coacervates (open-circle and cross patterns, respectively) or, alternatively, nucleation from a metastable parent phase (no pattern). The circled labels indicate the correspondence with the experimentally determined regions shown in panels A–D.

The overall topology of the phase diagram in Fig. 3E, and in particular the diagonal phase boundary between three-phase coexistence and NS+PLL coacervates at low salt concentrations, agrees with the experimental observations. The model also predicts that PLL is enriched in the condensed phase relative to the dilute phase at high salt concentrations ($\rho_S \gg \rho_U$) at equilibrium, although to a lesser extent than pNSs since phase separation is primarily driven by basepairing interactions under these conditions (Fig. S8). This prediction is consistent with the long-time behavior of the pNS-dominated droplets at 2.5 M NaCl, as noted above.

Explaining the precise experimental conditions under which three-phase coexistence is observed requires us to consider kinetic effects in addition to equilibrium phase behavior. According to our model, the three-phase region seen in Fig. 3C extends at equilibrium into the regions probed in Fig. 3B and, to a lesser extent, into Fig. 3D. However, the model also predicts that phase separation from an initially homogeneous solution proceeds via spinodal decomposition, since the minimum-free-energy path from the parent concentration to one or both of the condensed phases is entirely downhill on the free-energy landscape. The phase behavior that is observed on the timescales considered in the experiments is thus likely to be strongly influenced by the first condensed phase to

form, especially considering the exceedingly slow kinetics at both high and low salt concentrations. For this reason, it is likely that the liquid-like droplets in Fig. 3B are the result of spinodal decomposition to a condensed phase that incorporates both pNS and PLL, is stabilized by both homotypic and heterotypic interactions, and does not facilitate further equilibration into immiscible condensed phases. By contrast, at low salt concentrations ($\rho_S \lesssim \rho_U$) and excess polyanion, the model predicts that the minimum-free-energy paths to both condensed phases traverse free-energy barriers, indicating that condensation must occur via nucleation. This mechanism is more likely to produce distinct droplets of two immiscible condensed phases, leading to the direct observation of three-phase coexistence in Fig. 3C. Taken together, these various lines of evidence suggest that the phase behavior in Fig. 3A–D is the product of both thermodynamic and kinetic effects, which in turn both depend on the balance between homotypic and heterotypic interactions at different macromolecular compositions and salt concentrations.

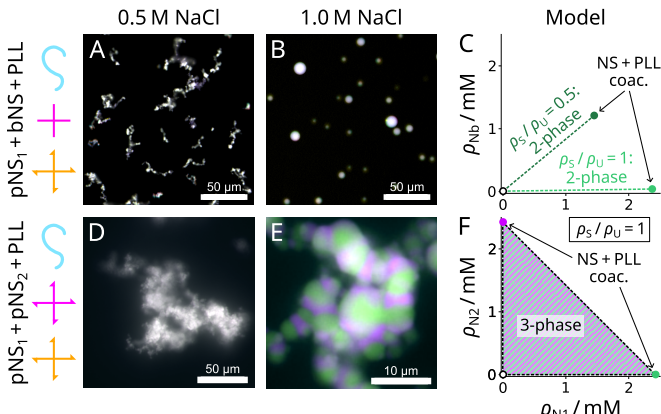


Figure 4. Variable-composition and multiphase NS+PLL coacervates at 25 °C. Mixtures of blunt NS (5 μM bNS, magenta), pNS (5 μM , yellow), and PLL (19.2 μM , cyan) form (A) three-component, kinetically arrested coacervate gels at 0.5 M NaCl and (B) three-component liquid-like coacervates at 1 M NaCl. Note that regions where magenta, cyan, and yellow colocalize appear gray (see also Fig. S9). (C) Equilibrium theoretical phase diagrams predict a shift from roughly equal bNS concentration, ρ_{N1} , and pNS concentration, ρ_{N2} , in the coacervate at low salt concentrations to greater pNS partitioning at higher salt concentrations near $\rho_S = \rho_U$. (D) Mixtures comprising two palindromic NSs with orthogonal sticky-end sequences, pNS₁ and pNS₂, also form three-component, kinetically arrested coacervate gels with PLL at 0.5 M NaCl (5 μM pNS₁, magenta; 5 μM pNS₂, yellow; 19.2 μM PLL, cyan). (E) At 1 M NaCl, each pNS species forms liquid-like coacervates with PLL, but these condensed phases are immiscible with one another. (F) The equilibrium theoretical phase diagram at $\rho_S = \rho_U$ predicts three-phase coexistence, in which two distinct NS+PLL coacervate phases enriched in pNS₁ and pNS₂, respectively, coexist with a dilute phase. Note that panels C and F show projections of the phase diagrams with the parent concentration fixed to the experimental concentrations in panels A,B and D,E, respectively.

G. Sequence-dependent NS partitioning into immiscible coacervates

Finally, we asked whether the interplay among homotypic and heterotypic interactions can be used to assemble immiscible pNS+PLL coacervates enriched in distinct NS species. Prior works have demonstrated the formation of immiscible pNS phases through the use of orthogonal palindromic sticky-end sequences that have no affinity for one another [13, 35]. However, in those cases, homotypic base pairing provided the sole driving force for phase separation. Here, we instead consider the formation of multicomponent coacervates and investigate whether the heterotypic interactions involving the shared PLL component overwhelm the homotypic interactions, driving the distinct pNS phases to mix.

To this end, we first studied a mixture of PLL, pNS, and blunt NS (bNS) at a 1:1/2:1/2 macromolecular charge ratio. The bNS species has no sticky ends and thus does not contribute homotypic interactions. At 0.5 M

NaCl, this mixture forms kinetically arrested coacervate gels incorporating all three macromolecular components, including both NS species, likely due to the dominant role of electrostatic interactions at this salt concentration (Fig. 4A and Fig. S9). At 1 M NaCl, the three macromolecular components assemble into liquid-like droplets (Fig. 4B and Fig. S9). However, closer examination of the compositions of these droplets revealed greater partitioning of the pNS species at this salt concentration (Fig. S10). This finding is consistent with our previous conclusion that basepairing interactions are needed to stabilize droplets under these conditions (cf. Fig. 1D), since only the pNS species provides this homotypic contribution to the driving force for phase separation and can therefore be expected to be enriched in the multicomponent droplets to a greater extent. This expectation is corroborated by our model, which predicts a shift in the equilibrium droplet NS composition from roughly equimolar pNS and bNS when $\rho_S < \rho_U$ to predominantly pNS when $\rho_S \gtrsim \rho_U$ (Fig. 4C). We emphasize that this compositional shift is a consequence of the electrostatic heterotypic interactions, since bNSs are predicted to be excluded from the condensed phase at all salt concentrations in the absence of PLL (Fig. S11).

We then considered a mixture of PLL and two distinct pNS species with orthogonal palindromic sequences, pNS₁ (5'-CGATCG-3') and pNS₂ (5'-GCTAGC-3'), at a 1:1/2:1/2 macromolecular charge ratio. Although a single kinetically arrested coacervate gel was observed at 0.5 M NaCl (Fig. 4D and Fig. S9), phase separation led to the formation of two immiscible liquid-like coacervates at 1 M NaCl (Fig. 4E and Fig. S9). PLL is enriched in both of these coacervates, but each is enriched in a single pNS species, with the orthogonal pNS species excluded. The two condensed phases were found to adhere strongly to one another, presumably due to the shared PLL component, and to coarsen over time while remaining immiscible (Fig. S12). These observations are also consistent with our theoretical model, which predicts equilibrium three-phase coexistence between a dilute phase, a pNS₁+PLL condensed phase, and a pNS₂+PLL condensed phase when $\rho_S \simeq \rho_U$ (Fig. 4F). We therefore conclude that heterotypic interactions can indeed dominate over orthogonal homotypic interactions, but in a manner that is highly tunable with salt: at intermediate salt concentrations, the weakened heterotypic attractions allow for base pairing-driven demixing of the two pNS species while still supplying the driving force for pNS₁+PLL and pNS₂+PLL coacervation (Fig. S11). Importantly, the transition from a three-component coacervate to two two-component coacervates occurs due to the same cooperativity between electrostatics and base pairing that is necessary for pNS+PLL coacervation at intermediate salt concentrations.

III. CONCLUSIONS

Through a combination of experiments and theoretical calculations, we have shown how the interplay between heterotypic electrostatics and homotypic basepairing interactions govern the phase behavior of mixtures of nucleic acids and charged polypeptides. By controlling the sticky-end sequences, salt concentration, temperature, and macromolecular composition, we have been able to distinguish contributions to the overall driving force for phase separation arising from each of these interaction modalities. These systems exhibit surprisingly complex phase behavior in the intermediate salt regime, where the magnitudes of the heterotypic and homotypic interactions are comparable due to the opposite effects of added salt on electrostatics and base pairing. Both the equilibrium phase behavior and the nonequilibrium kinetics of phase separation can be rationalized to a large extent by our theoretical model, without the need for fitting parameters.

Our work reveals how electrostatic and basepairing interactions can either cooperate or compete with one another to shape the phase behavior of mixtures of nucleic acid and charged polypeptides. On the one hand, these interaction modalities cooperate to increase the range of salt concentrations and temperatures at which coacervation can occur, most strikingly at high temperatures and high salt concentrations at which neither interaction modality is sufficient to drive phase separation on its own. On the other hand, the observation of three-phase coexistence in mixtures with a single pNS species and PLL indicates that these interaction modalities can also compete, leading to the formation of distinct condensed phases that are individually dominated by one or the other type of interaction. Competition between homotypic and heterotypic interactions is also responsible for the demixing of coacervate phases in mixtures of multiple pNS species with orthogonal sticky ends and PLL. These conclusions are broadly compatible with the recent findings of Ohno *et al.* [36]. Importantly, our synthesis of experiments and theoretical calculations allows us to explain how these qualitative changes in both the equilibrium phase behavior and the nonequilibrium phase-separation kinetics arise from relatively subtle changes in the solution conditions.

Notably, these varied phase behaviors were all observed at easily accessible salt concentrations at room temperature. In particular, for the specific pNS and PLL constructs studied in this work, the intermediate salt range at which the heterotypic and homotypic interactions become comparable to one another is located below 1 M NaCl. Our work therefore suggests that physiological solutions of nucleic acids and polypeptides are naturally poised to exhibit complex and easily tunable phase behaviors due to the comparable strengths of heterotypic and homotypic interactions arising from electrostatics and base pairing.

IV. METHODS

A. NS formation

DNA oligomers were ordered from IDT with standard desalting purification (sequences given in Table S1). They were resuspended in 10 mM Tris-HCl before being mixed at equimolar concentrations. The mixture was then annealed by heating at 95 °C for 10 minutes and then cooled to 4 °C at -0.5 °C/min. NSs were purified using 0.22 µm PVDF and 30 kDa regenerated cellulose centrifugal filters (Millipore Sigma and Amicon, respectively). Proper NS formation was confirmed using agarose gel electrophoresis (3% agarose gel with TBE running buffer). NSs were stored at -20 °C between experiments and incubated at 50 °C before use to dissolve any condensed phase formed at low temperature.

B. Sample preparation and visualization

10 mM Tris-HCl, 5 M NaCl, and water were combined and vortexed. Then monodisperse PLL (Alamanda Polymers, $n = 100$ unless otherwise stated) was added and pipette mixed. Finally, the NSs (5% tagged with respective fluorophore) were added to solution with a cut pipette tip and the solution was pipette mixed three times. If multiple species of NSs were included, they were combined before being added to the salt-PLL mixture such that all NSs were added in a single step.

NS+PLL samples were measured in a flow channel constructed from parafilm sandwiched between polyacrylamide coated glass slides, prepared following Ref. [37]. Briefly, microscope slides and coverslips were heavily cleaned by sonicating with Hellmanex, ethanol, NaOH, and water. Slides were then incubated for 30 minutes in 3-(Trimethoxysilyl)propyl methacrylate, ethanol, and acetic acid. Slides were coated by leaving them in solution with acrylamide, TEMED, and ammonium persulfate overnight. Immediately before use, slides were rinsed with water and dried with pure N₂ gas. Parafilm was melted onto the slide with a soldering iron such that a narrow channel was formed. Samples were added to the channel with a cut pipette tip to reduce shearing. Channels were sealed using Norland Optical Adhesive and that was cured with a UV light. Samples were immediately visualized using epifluorescent microscopy (Nikon Eclipse Ti2-E). Unless otherwise stated, samples were visualized at 25 °C (Oko UNO).

C. Theoretical model

In our model, each NS is represented as a single coarse-grained unit, referred to as a “blob”. Each PLL molecule is represented as a freely jointed chain of $N_p = 10$ Kuhn-length blobs [38]. Each blob carries a Gaussian charge

distribution,

$$q_i(r) = Z_i e \left(\frac{1}{2\pi\sigma_i^2} \right)^{\frac{3}{2}} \exp(-r^2/2\sigma_i^2), \quad (1)$$

where we use the subscript i to indicate the nanostar (N) and PLL (P) species. A blob of species i carries a total charge of $Z_i e$, where the blob radius σ_i describes the spatial range of the charge distribution. Microcations (+) and microanions (-), including counterions and added monovalent salt, are treated as point particles. We do not distinguish between these different sources of microions in the model. The implicit solvent is treated as a continuum. The number densities of these four ion species, ρ_N , ρ_P , ρ_+ , and ρ_- , are constrained by the electroneutrality condition

$$Z_N \rho_N + N_P Z_P \rho_P + \rho_+ - \rho_- = 0. \quad (2)$$

We construct a mean-field model by adapting the DLVO theory [39, 40] for colloidal particles to soft blobs. We then account for associative interactions between sticky ends using Wertheim's first-order perturbation theory [41]. This approach can be derived from the classical partition function of the blob mixture using classical density functional theory and mean-field approximations that treat the screened electrostatic and associative interactions on equal footing. This consistency between the treatment of electrostatic and basepairing interactions is crucial for the prediction of overlapping upper and lower critical salt concentrations for npNS+PLL coacervation and pNS associative phase separation, respectively. Complete details are provided in Sections S1-S4..

The total free-energy density of the mixture can be written as

$$f = f_{\text{poly}} + f_{\text{micro}} + f_{\text{self}} + f_{\text{assoc}}. \quad (3)$$

The first term represents the polyion reference state, consisting of a mixture of NSs and PLL with excluded volume interactions only. Following our prior work [42], the sum of the ideal and excluded-volume contributions for the polyions only is

$$\begin{aligned} \beta f_{\text{poly}} = & \rho_N \ln(\rho_N v_N) + \rho_P \ln \left(\frac{\rho_P N_P v_P}{1 - \rho_N v_N} \right) \\ & + \left(\frac{1 - \rho_N v_N}{v_N} \right) \ln(1 - \rho_N v_N) \\ & + \left(\frac{\phi_0}{v_P} \right) \ln \left(\frac{\phi_0}{1 - \rho_N v_N} \right), \end{aligned} \quad (4)$$

where $\beta \equiv (k_B T)^{-1}$, $v_N = 4\pi\sigma_N^3/3 = 524 \text{ nm}^3$ and $v_P = 4\pi\sigma_P^3/3 = 0.904 \text{ nm}^3$ are the volumes of N and P blobs, respectively, and $\phi_0 \equiv 1 - \rho_N v_N - \rho_P N_P v_P$ is the solvent-occupied volume fraction. In the absence of electrostatic interactions, microions also make ideal and excluded-volume contributions,

$$\begin{aligned} \beta f_{\text{micro}} = & \rho_+ \ln(\rho_+ v_0) + \rho_- \ln(\rho_- v_0) \\ & - (\rho_+ + \rho_-) \ln(1 - \eta). \end{aligned} \quad (5)$$

The volume v_0 of the microion point particles is included for dimensional consistency, although its value does not affect phase-coexistence calculations. The last term in f_{micro} accounts for the exclusion of microions from sterically inaccessible regions within the polyion blobs [43]. The total volume fraction of the system that is inaccessible to microions is

$$\eta = f_N \rho_N v_N + f_P \rho_P N_P v_P, \quad (6)$$

where $f_N \approx 0.01$ and $f_P \approx 0.5$ are the inaccessible fractions of the N and P blob volumes, respectively (Table S2).

At the mean-field level, the electrostatic interactions among all the solvated species reduce to a "self-energy" resulting from the formation of the electrical double layer, in which each polyion is immersed in an oppositely charged cloud of microions. The electrostatic contribution to the free-energy density is thus

$$\begin{aligned} \beta f_{\text{self}} = & -\frac{\kappa l_B}{2} \left[\rho_N Z_N^2 \exp(\kappa^2 \sigma_N^2) \operatorname{erfc}(\kappa \sigma_N) \right. \\ & \left. + N_P \rho_P Z_P^2 \exp(\kappa^2 \sigma_P^2) \operatorname{erfc}(\kappa \sigma_P) \right], \end{aligned} \quad (7)$$

where $l_B = 0.71 \text{ nm}$ is the Bjerrum length in aqueous solution and $\kappa = [4\pi l_B (\rho_+ + \rho_-)]^{1/2}$ is the inverse Debye screening length. Notably, this contribution to the free energy has no explicit temperature dependence, whereas the salt concentration affects κ .

The associative contribution to the free energy is [41]

$$\beta f_{\text{assoc}} = m \rho_N \left(\ln X - \frac{X}{2} + \frac{1}{2} \right), \quad (8)$$

where $m = 4$ is the number of sticky ends per pNS and X is the probability that an individual sticky end on a pNS is unbound,

$$X = \frac{-1 + \sqrt{1 + 4\rho_N v_N \Delta}}{2\rho_N v_N \Delta}. \quad (9)$$

The dimensionless sticky-end association strength, Δ , is related to the hybridization free energy, ΔG , of sticky-end oligonucleotides that are free in solution via

$$\Delta = \frac{m\Omega}{4\pi} \exp(-\beta \Delta G) v_N^{-1} \cdot M^{-1}, \quad (10)$$

where $\Omega = \pi/4$ is the solid angle accessible to a sticky-end on a pNS blob [44], and the oligonucleotide hybridization free energies are reported relative to a standard concentration of 1 M [23]. Standard ΔG° values were computed as a function of temperature at 1 M NaCl using NUPACK [45]. These standard values were reduced by $3.06 k_B T$ to avoid double counting of salt effects, which are also accounted for implicitly in the NUPACK predictions. An experimentally validated empirical salt correction [23] was then applied to obtain a salt-dependent association strength,

$$\Delta = \Delta_0 (\rho_+ \cdot M^{-1})^\alpha, \quad (11)$$

where $\Delta_0 = \Delta(\Delta G^\circ)$ is the association strength at 1 M monovalent cation concentration and $\alpha = 1.15$. The association contribution to the free energy therefore depends explicitly on both temperature and salt concentration via the association strength Δ .

Importantly, all parameters for this model are determined based on their physical values or prior measurements, leaving no fitting parameters for comparison with the experiments reported in this work. Phase diagrams were computed by first finding the convex hull of the free-energy density as a function of ρ_N , ρ_P , and ρ_S and then refining the boundaries of the coexistence regions and the predicted tie lines by explicitly solving for equal chemical potentials for all species and equal pressures in all coexisting phases. Kinetic pathways were predicted between an initial homogeneous solution at the parent concentra-

tion and each of the (meta)stable phases by calculating the minimum-free-energy path on the free-energy landscape using the string method [46]. Complete details of these numerical methods are provided in Sections S1-S4.

ACKNOWLEDGMENTS

Research reported in this publication was supported by the the National Science Foundation under award number DMR-2005189 to OAS and DMR-2143670 to WMJ; by an award from the W.M. Keck Foundation to OAS; and by the National Institute of General Medical Sciences of the National Institutes of Health under award number R35GM155017 to WMJ.

[1] B. R. Sabari, A. Dall’Agnese, and R. A. Young, Biomolecular condensates in the nucleus, *Trends Biochem. Sci.* , 961–977 (2020).

[2] D. Campos-Melo, Z. C. Hawley, C. A. Doppelmann, and M. J. Strong, The integral role of RNA in stress granule formation and function, *Front. Cell Dev. Biol.* **9**, 808 (2021).

[3] L. Peng, E. M. Li, and L. Y. Xu, From start to end: Phase separation and transcriptional regulation, *Biochim. Biophys. Acta Gene Regul. Mech.* **1863**, 194641 (2020).

[4] L. Wan, J. Ke, Y. Zhu, W. Zhang, and W. Mu, Recent advances in engineering synthetic biomolecular condensates, *Biotechnol. Adv.* **77**, 108452 (2024).

[5] Y. Song, Liquid–liquid phase separation-inspired design of biomaterials, *Biomaterials Science* **12**, 1943 (2024).

[6] S. Lim and D. S. Clark, Phase-separated biomolecular condensates for biocatalysis, *Trends Biotechnol.* **42**, 496 (2024).

[7] P. Li, S. Banjade, H.-C. Cheng, S. Kim, B. Chen, L. Guo, M. Llaguno, J. V. Hollingsworth, D. S. King, S. F. Bannani, *et al.*, Phase transitions in the assembly of multivalent signalling proteins, *Nature* **483**, 336 (2012).

[8] E. W. Martin, A. S. Holehouse, I. Peran, M. Farag, J. J. Incicco, A. Bremer, C. R. Grace, A. Soranno, R. V. Pappu, and T. Mittag, Valence and patterning of aromatic residues determine the phase behavior of prion-like domains, *Science* **367**, 694 (2020).

[9] A. Chowdhury, A. Borgia, S. Ghosh, A. Sottini, S. Mitra, R. S. Eapen, M. B. Borgia, T. Yang, N. Galvanetto, M. T. Ivanović, *et al.*, Driving forces of the complex formation between highly charged disordered proteins, *Proc. Natl. Acad. Sci. U. S. A.* **120**, e2304036120 (2023).

[10] A. Jain and R. D. Vale, RNA phase transitions in repeat expansion disorders, *Nature* **546**, 243 (2017).

[11] S. Biffi, R. Cerbino, F. Bomboi, M. Paraboschi, R. As-selta, F. Sciortino, and T. Bellini, Phase behavior and critical activated dynamics of limited-valence DNA nanostars, *Proc. Natl. Acad. Sci. U. S. A.* **110**, 15633 (2013).

[12] B. J. Jeon, D. T. Nguyen, G. R. Abraham, N. Conrad, D. K. Fygenson, and O. A. Saleh, Salt-dependent properties of a coacervate-like, self-assembled DNA liquid, *Soft Matter* **14**, 7009 (2018).

[13] Y. Sato, T. Sakamoto, and M. Takinoue, Sequence-based engineering of dynamic functions of micrometer-sized DNA droplets, *Sci. Adv.* **6**, eaba3471 (2020).

[14] D. T. Nguyen and O. A. Saleh, Tuning phase and aging of DNA hydrogels through molecular design, *Soft Matter* **13**, 5421 (2017).

[15] T. Lee, S. Do, J. G. Lee, D.-N. Kim, and Y. Shin, The flexibility-based modulation of DNA nanostar phase separation, *Nanoscale* **13**, 17638 (2021).

[16] N. Conrad, G. Chang, D. K. Fygenson, and O. A. Saleh, Emulsion imaging of a dna nanostar condensate phase diagram reveals valence and electrostatic effects, *The Journal of Chemical Physics* **157**, 234203 (2022).

[17] N. Conrad, T. Kennedy, D. K. Fygenson, and O. A. Saleh, Increasing valence pushes DNA nanostar networks to the isostatic point, *Proc. Natl. Acad. Sci. U. S. A.* **116**, 7238 (2019).

[18] E. Bianchi, J. Largo, P. Tartaglia, E. Zaccarelli, and F. Sciortino, Phase diagram of patchy colloids: Towards empty liquids, *Phys. Rev. Lett.* **97**, 168301 (2006).

[19] W. A. Wee, H. Sugiyama, and S. Park, Photoswitchable single-stranded DNA-peptide coacervate formation as a dynamic system for reaction control, *iScience* **24**, 103455 (2021).

[20] Y. Yin, L. Niu, X. Zhu, M. Zhao, Z. Zhang, S. Mann, and D. Liang, Non-equilibrium behaviour in coacervate-based protocells under electric-field-induced excitation, *Nat. Commun.* **7**, 1 (2016).

[21] J. R. Vieregg, M. Lueckheide, A. B. Marciel, L. Leon, A. J. Bologna, J. R. Rivera, and M. V. Tirrell, Oligonucleotide-peptide complexes: Phase control by hybridization, *J. Am. Chem. Soc.* **140**, 1632 (2018).

[22] G. M. Wadsworth, W. J. Zahurancik, X. Zeng, P. Pullara, L. B. Lai, V. Sidharthan, R. V. Pappu, V. Gopalan, and P. R. Banerjee, RNAs undergo phase transitions with lower critical solution temperatures, *bioRxiv* , 2022 (2022).

[23] J. SantaLucia Jr and D. Hicks, The thermodynamics of DNA structural motifs, *Annu. Rev. Biophys. Biomol. Struct.* **33**, 415 (2004).

[24] J. R. Vieregg, M. Lueckheide, A. B. Marciel, L. Leon, A. J. Bologna, J. R. Rivera, and M. V. Tirrell, Oligonucleotide-peptide complexes: phase control by hybridization, *J. Am. Chem. Soc.* **140**, 1632 (2018).

[25] Q. Wang and J. B. Schlenoff, The polyelectrolyte complex/coacervate continuum, *Macromolecules* **47**, 3108 (2014).

[26] L. M. Jawerth, M. Ijavi, M. Ruer, S. Saha, M. Jahnel, A. A. Hyman, F. Jülicher, and E. Fischer-Friedrich, Salt-dependent rheology and surface tension of protein condensates using optical traps, *Phys. Rev. Lett.* **121**, 258101 (2018).

[27] J. Yuan and H. Tanaka, Network-forming phase separation of oppositely charged polyelectrolytes forming coacervates in a solvent, *Nat. Commun.* **16**, 1517 (2025).

[28] J.-P. Hansen, D. Coslovich, and G. Kahl, Effective interactions between oppositely charged polyelectrolytes in the presence of salt, *Mol. Phys.* **109**, 2953 (2011).

[29] W. G. Chapman, K. E. Gubbins, G. Jackson, and M. Radosz, Saft: Equation-of-state solution model for associating fluids, *Fluid Phase Equilib.* **52**, 31 (1989).

[30] L. Rovigatti, F. Bomboi, and F. Sciortino, Accurate phase diagram of tetravalent dna nanostars, *The Journal of Chemical Physics* **140**, 154903 (2014).

[31] D. G. Archer and P. Wang, The dielectric constant of water and debye-hückel limiting law slopes, *J. Phys. Chem. Ref. Data* **19**, 371 (1990).

[32] E. Locatelli, P. H. Handle, C. N. Likos, F. Sciortino, and L. Rovigatti, Condensation and demixing in solutions of DNA nanostars and their mixtures, *ACS Nano* **11**, 2094 (2017).

[33] C. E. Sing, Development of the modern theory of polymeric complex coacervation, *Adv. Colloid Interface Sci.* **239**, 2 (2017).

[34] S. Ali, M. Bleuel, and V. M. Prabhu, Lower critical solution temperature in polyelectrolyte complex coacervates, *ACS Macro Lett.* **8**, 289 (2019).

[35] B. J. Jeon, D. T. Nguyen, and O. A. Saleh, Sequence-controlled adhesion and microemulsification in a two-phase system of DNA liquid droplets, *J. Phys. Chem. B* **124**, 8888 (2020).

[36] H. Ohno, J. Kijima, Y. Ochi, M. Shoji, J. Taira, T. Mabuchi, and Y. Sato, Oligolysine enhances and inhibits DNA condensate formation, *ACS Omega* **10**, 15781 (2025).

[37] S. J. DeCamp, G. S. Redner, A. Baskaran, M. F. Hagan, and Z. Dogic, Orientational order of motile defects in active nematics, *Nat. Mater.* **14**, 1110 (2015).

[38] L. Shi, F. Carn, F. Boué, G. Mosser, and E. Buhler, Control over the electrostatic self-assembly of nanoparticle semiflexible biopolyelectrolyte complexes, *Soft Matter* **9**, 5004 (2013).

[39] B. V. Derjaguin, Theory of the stability of strongly charged lyophobic sol and of the adhesion of strongly charged particles in solutions of electrolytes, *Acta Phys. Chim. URSS* **14**, 633 (1941).

[40] E. J. W. Verwey, Theory of the stability of lyophobic colloids., *J. Phys. Chem.* **51**, 631 (1947).

[41] M. S. Wertheim, Fluids with highly directional attractive forces. I. Statistical thermodynamics, *J. Stat. Phys.* **35**, 19 (1984).

[42] T. Li, W. B. Rogers, and W. M. Jacobs, Interplay between self-assembly and phase separation in a polymer-complex model, *Phys. Rev. E* **108**, 064501 (2023).

[43] B. Widom, Some topics in the theory of fluids, *J. Chem. Phys.* **39**, 2808 (1963).

[44] O. Hegde, T. Li, A. Sharma, M. Borja, W. M. Jacobs, and W. B. Rogers, Competition between self-assembly and phase separation governs high-temperature condensation of a DNA liquid, *Phys. Rev. Lett.* **132**, 208401 (2024).

[45] M. E. Fornace, N. J. Porubsky, and N. A. Pierce, A unified dynamic programming framework for the analysis of interacting nucleic acid strands: Enhanced models, scalability, and speed, *ACS Synth. Biol.* **9**, 2665 (2020).

[46] W. E, W. Ren, and E. Vanden-Eijnden, Simplified and improved string method for computing the minimum energy paths in barrier-crossing events, *J. Chem. Phys.* **126**, 164103 (2007).

[47] R. van Roij, M. Dijkstra, and J.-P. Hansen, Phase diagram of charge-stabilized colloidal suspensions: van der Waals instability without attractive forces, *Phys. Rev. E* **59**, 2010 (1999).

[48] S. Biffi, R. Cerbino, F. Bomboi, E. M. Paraboschi, R. Asselta, F. Sciortino, and T. Bellini, Phase behavior and critical activated dynamics of limited-valence DNA nanostars, *Proc. Natl. Acad. Sci. U. S. A.* **110**, 15633 (2013).

[49] W. M. Jacobs, Theory and simulation of multiphase coexistence in biomolecular mixtures, *J. Chem. Theory Comput.* **19**, 3429 (2023).

[50] F. Gao and L. Han, Implementing the nelder-mead simplex algorithm with adaptive parameters, *Comput. Optim. Appl.* **51**, 259 (2012).

[51] J. J. Moré, B. S. Garbow, and K. E. Hillstrom, *User guide for MINPACK-1*, Tech. Rep. (CM-P00068642, 1980).

[52] S. Mao, D. Kuldinow, M. P. Haataja, and A. Košmrlj, Phase behavior and morphology of multicomponent liquid mixtures, *Soft Matter* **15**, 1297 (2019).

[53] J.-P. Hansen and I. R. McDonald, *Theory of Simple Liquids*, fourth edition ed. (Academic Press, Oxford, 2013).

SUPPLEMENTARY INFORMATION

SUPPLEMENTARY TABLE

Table S1: DNA sequences used in experiments. Fluorescent tags were included on the first oligo of each NS.

NS-oligo #	Sequence
pNS-1	CGA TCG ACG CTG CAA CTG GAG GAT ACG AAG CCG TGG CAA GTC AGG TGC G
pNS-2	CGA TCG ACG GCT CAG TCG GTT TCC GAG AAC GTA TCC TCC AGT TGC AGC G
pNS-3	CGA TCG ACG AGC GTT GGA CAT GTA TCG AAC TCG GAA ACC GAC TGA GCC G
pNS-4	CGA TCG ACG CAC CTG ACT TGC CAC GGC AAC GAT ACA TGT CCA ACG CTC G
npNS-1	GCG CGC GGG CAG TTC TCC GCT TCG CTC GCT CGT CGG CCG CGC
npNS-2	ACC TTC CTG CGC GCG GCT CGC ATT CCC GCG TTG GCA ATG GGC CTG GCG GCG CTT TCC AGA
npNS-3	GCG CCG CCA GGC CCA TTG CCT TGC GGA GAA CTG CCC GCG CGC TTT CCA GA
npNS-4	ACC TTC CTG CGC GCG GCC GAC GAG CGA GCG TTC GCG GGA ATG CGA GCC GCG C
Blunt NS-1	TCG CTG CAA CTG GAG GAT ACG AAG CCG TGG CAA GTC AGG TGC G
Blunt NS-2	TCG GCT CAG TCG GTT TCC GAG AAC GTA TCC TCC AGT TGC AGC G
Blunt NS-3	TCG AGC GTT GGA CAT GTA TCG AAC TCG GAA ACC GAC TGA GCC G
Blunt NS-4	TCG CAC CTG ACT TGC CAC GGC AAC GAT ACA TGT CCA ACG CTC G
pNS2-1	GCT AGC ACA CCG CCC GGG CAG AAC AGG AAC GGT GAT ATC CCG GGC CTC G
pNS2-2	GCT AGC ACT TCG CCC GGG TGC TAA GAG AAC CTG TTC TGC CCG GGC GGT G
pNS2-3	GCT AGC AGC CTT CCC GGG AGC GCT CGC AAC TCT TAG CAC CCG GGC GAA G
pNS2-4	GCT AGC ACG AGG CCC GGG ATA TCA CCG AAG CGA GCG CTC CCG GGA AGG C

SUPPLEMENTARY FIGURES

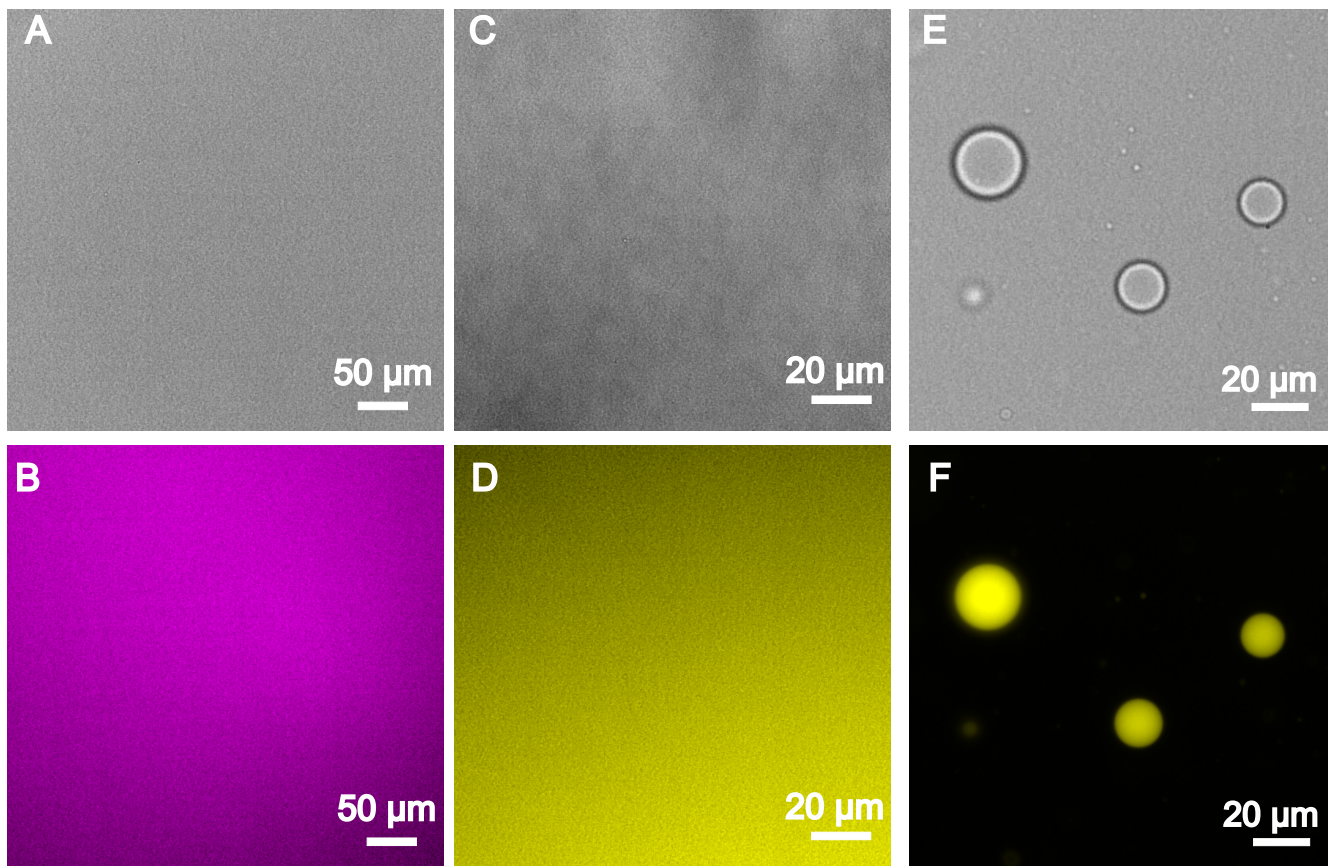


Figure S1. Representative images of NS phase behavior in the absence of PLL. (A,B) npNSs remain well mixed at 1 M NaCl, shown in (A) brightfield and (B) fluorescence. (C,D) pNSs do not phase separate at 75 mM NaCl, shown in (C) brightfield and (D) fluorescence. (E,F) pNSs phase separate at 1 M NaCl, shown in (E) brightfield and (F) fluorescence. All conditions contain 10 μ M NS.

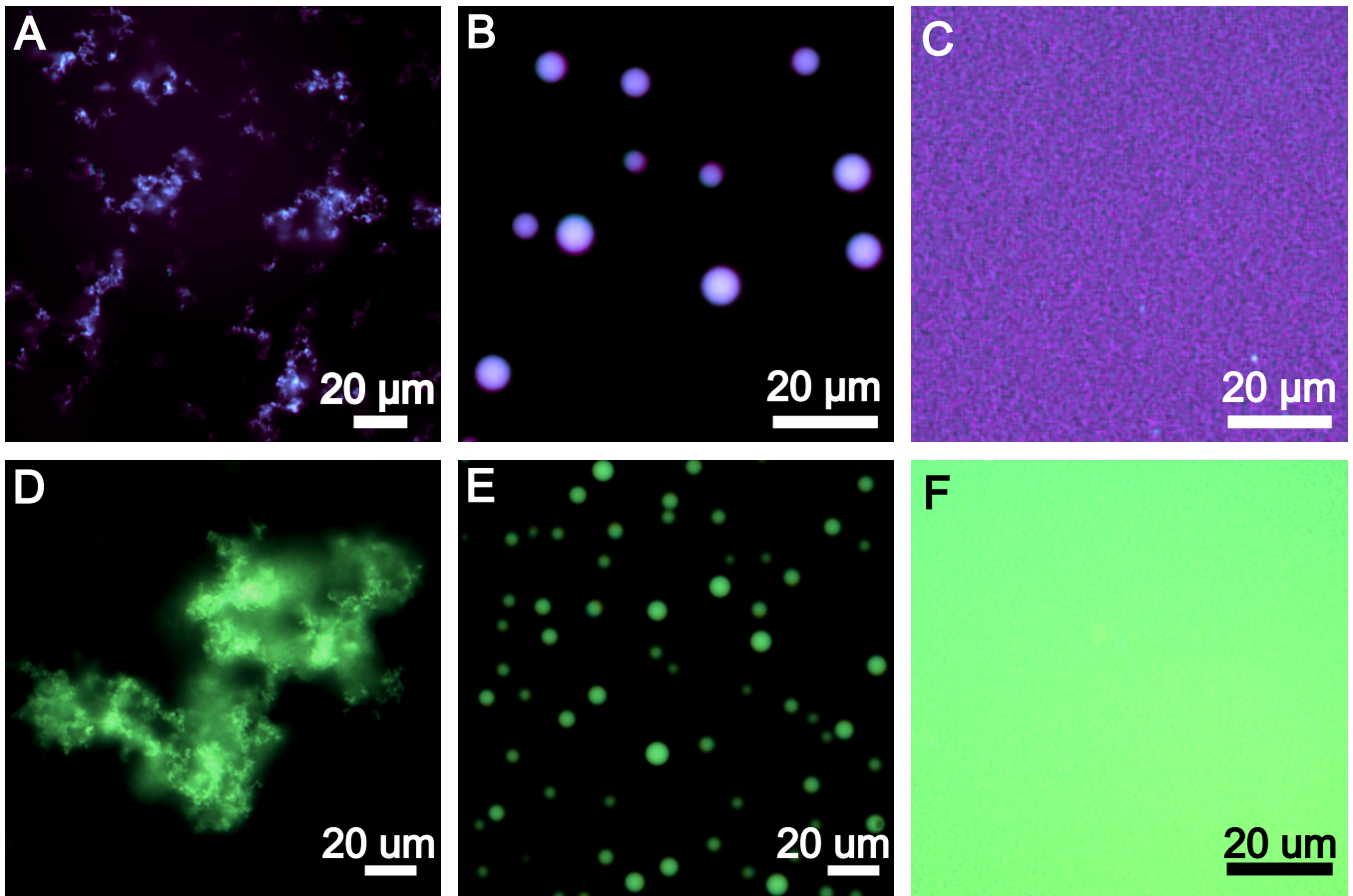


Figure S2. npNS+PLL and blunt NS+PLL phase separation. Blunt NS (magenta) and PLL (cyan) (A) form kinetically trapped gels at 0.25 M NaCl, (B) form drops at 0.5 M NaCl, and (C) remain well-mixed at 1 M NaCl. Similarly, npNSs with non-palindromic sticky ends (yellow) and PLL (D) form kinetically trapped gels at 0.25 M NaCl, (E) form drops at 0.5 M NaCl, and (F) remain well-mixed at 1 M NaCl.

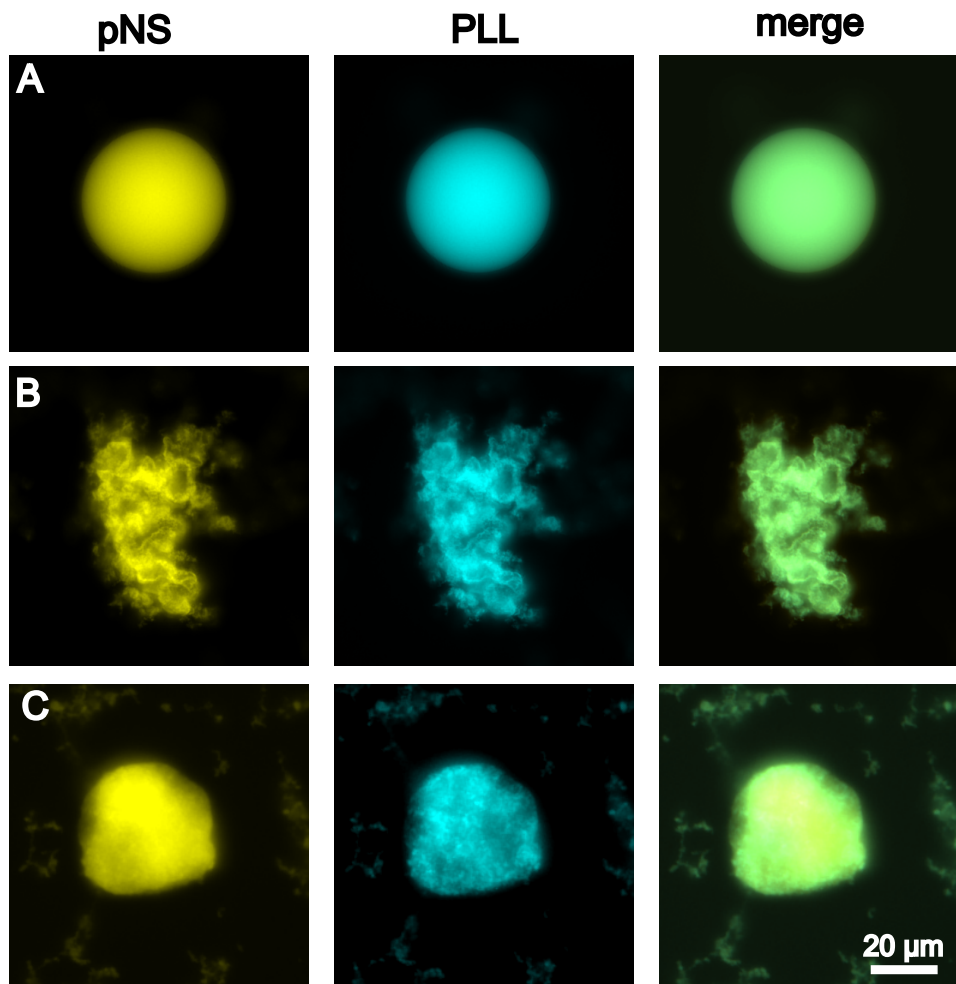


Figure S3. 2-channel fluorescent images of various pNS+PLL mixtures after 48 hours at room temperature. The condensed phase in each situation is similar to the images taken shortly after mixing, and in the corresponding condition, as shown in Fig. 3 in the main text; this indicates a lack of aging, and near-equilibrium behavior, in these conditions. (A) 1 M NaCl at 1:1 macromolecular charge ratio, (B) 0.5 M NaCl at $1/2:1$ macromolecular charge ratio, and (C) 0.25 M NaCl $1/4:1$ macromolecular charge ratio.

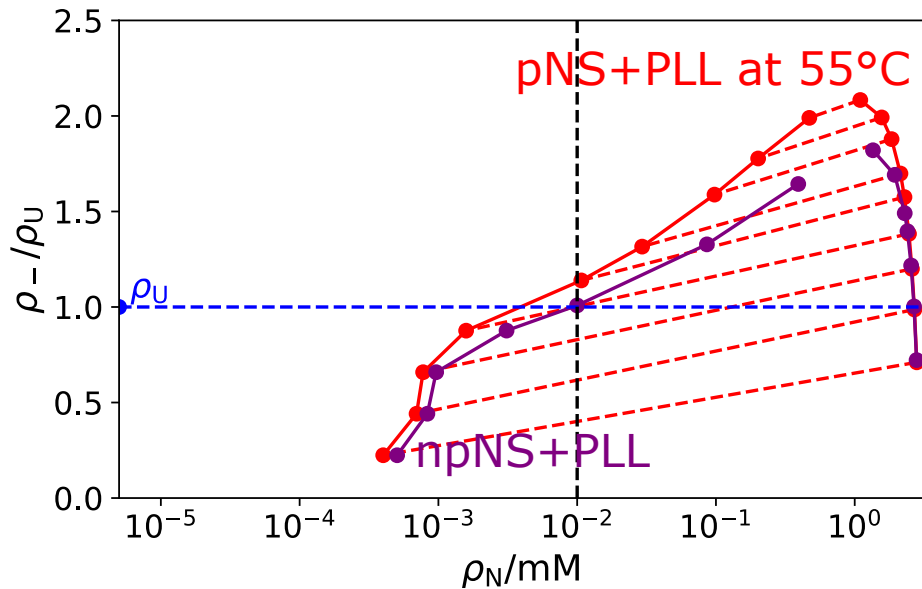


Figure S4. Comparison of predicted phase diagrams for the pNS+PLL and npNS+PLL systems at 55 °C. The increased upper transition salt concentration indicates cooperativity between electrostatic and basepairing interactions.

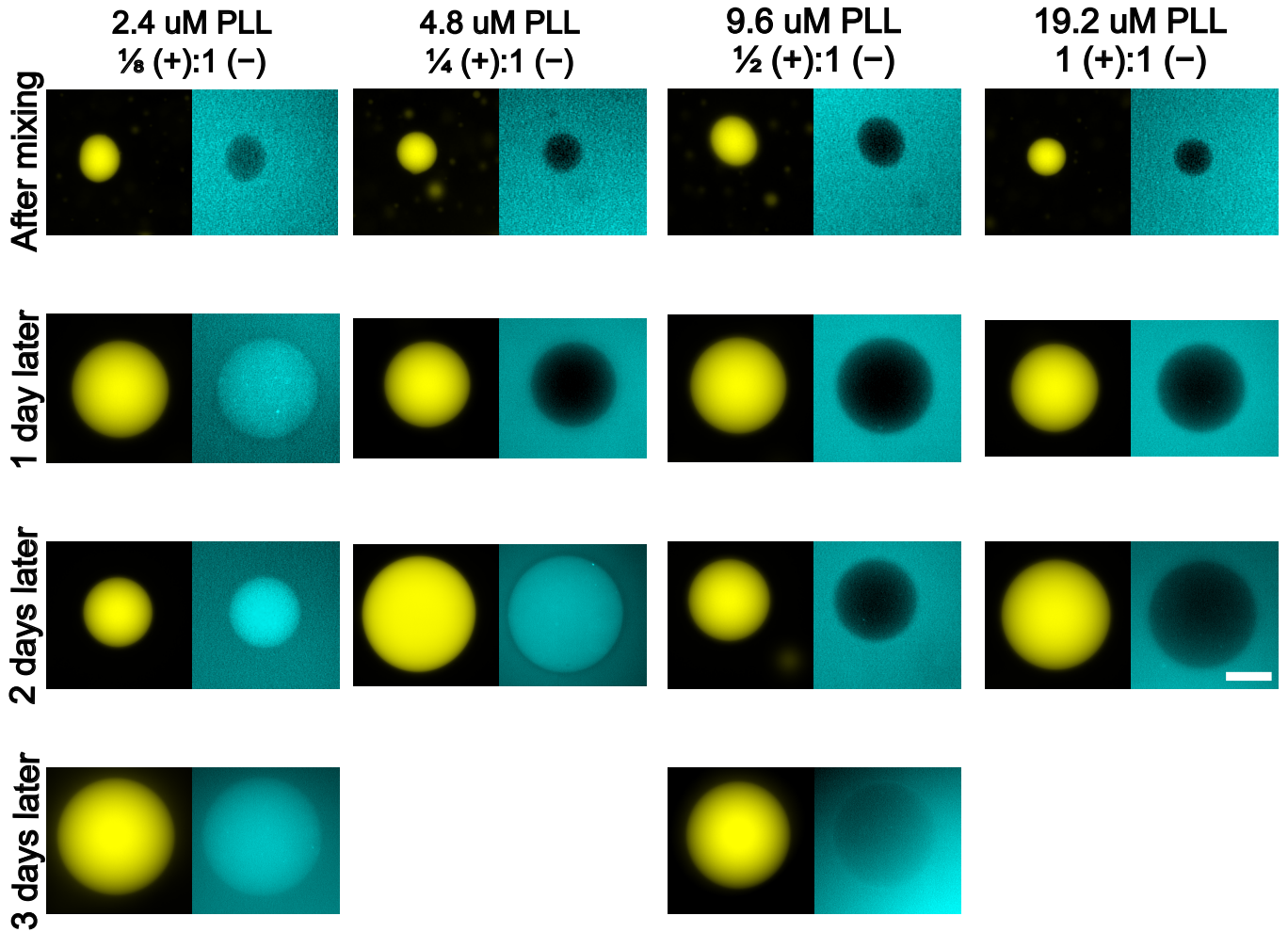


Figure S5. Fluorescent images of pNS (yellow) + PLL (cyan) mixtures at 2.5 M NaCl over time, showing slow dynamics of PLL partitioning, with timescales of hours to days. This figure shows that the timescale is sensitive to PLL concentration, with enrichment occurring more quickly in systems that are further from macromolecular charge balance. See Fig. S6 for data showing the sensitivity of enrichment timescale to PLL length. It is surprising that such slow timescales are observed at very high salt, as one might have guessed that the reduced electrostatic interactions would permit PLL to move relatively quickly through a DNA matrix. We speculate that a coacervate membrane might be forming around the pNS droplets shortly after their formation, and that membrane might impede further PLL penetration. This hypothesis could also potentially explain why longer PLL penetrates more slowly, as the membrane might be more stable due to more extensive entanglement of longer PLL with the DNA. Scale bars = 20 μ m.

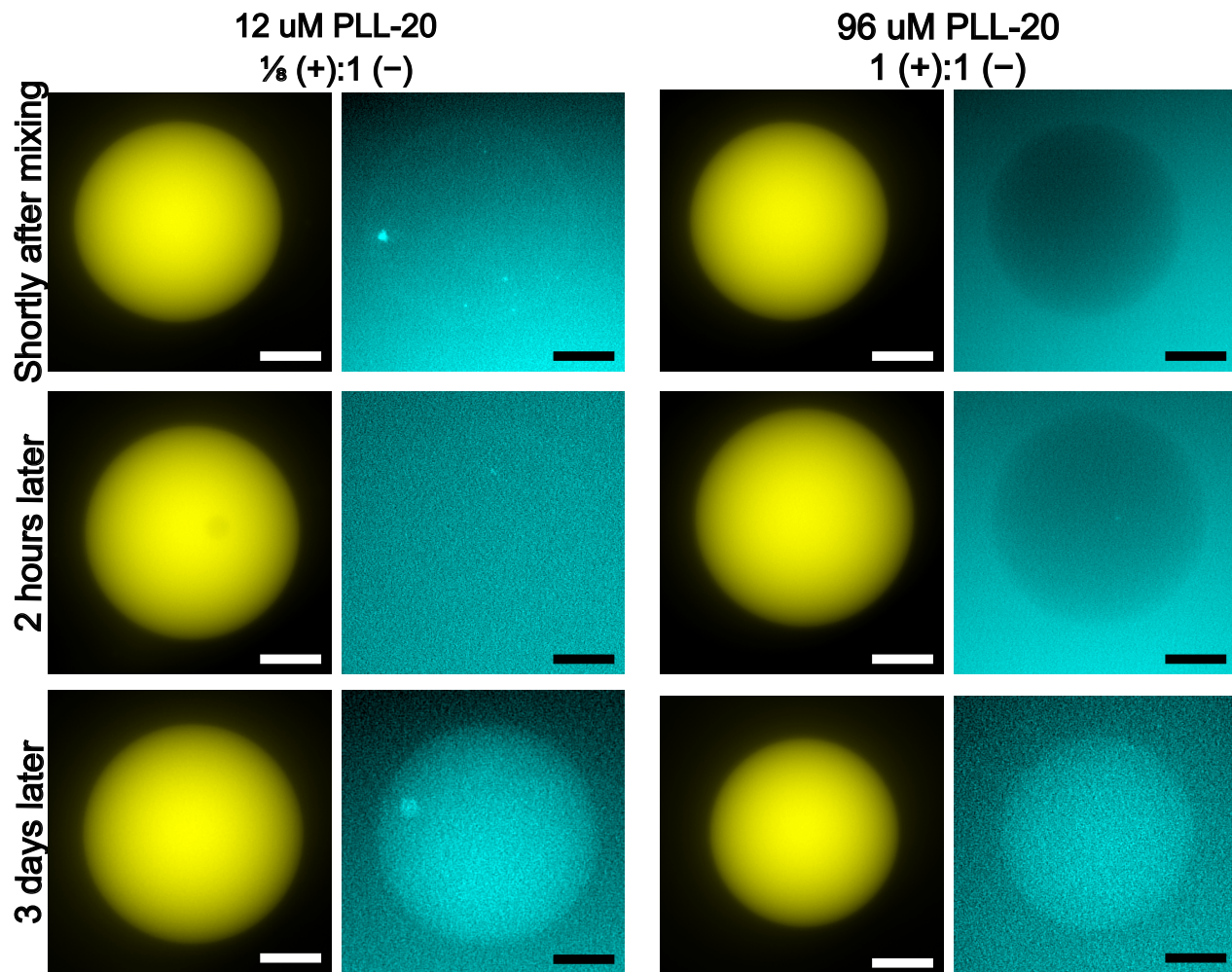


Figure S6. PLL₂₀ (20 residues) partitions faster than PLL₁₀₀ (100 residues) at 2.5 M NaCl. *Left:* At a 1/8:1 macromolecular charge ratio, PLL₂₀ is roughly equally concentrated in the dense and dilute phases after two hours, then becomes slightly enriched after three days. *Right:* At a 1:1 macromolecular charge ratio, PLL₂₀ is excluded shortly after mixing and two hours later, and then becomes slightly enriched within three days. Scale bars = 10 μ m.

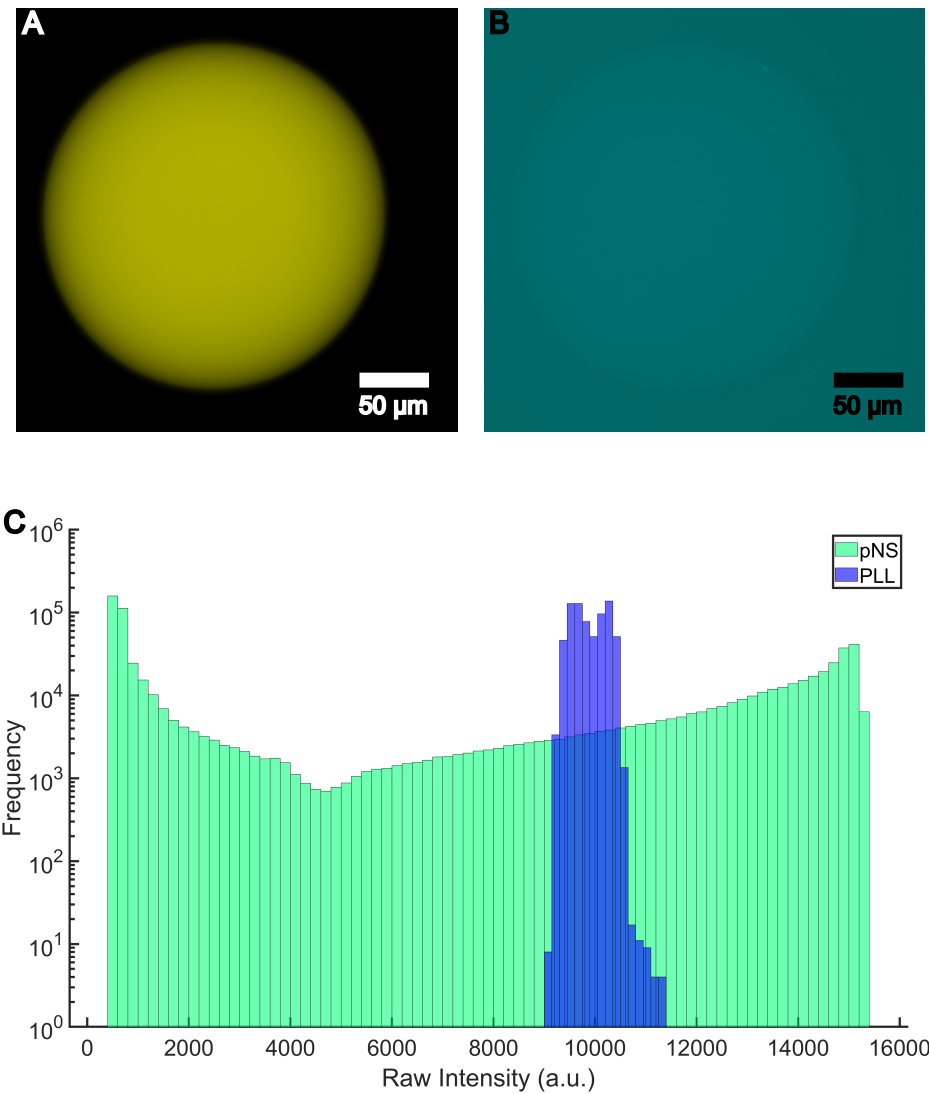


Figure S7. The partition coefficients of pNSs are higher than for PLL after three days of incubation at 2.5 M NaCl. Representative images of (A) pNS (yellow) and (B) PLL (cyan) at a 1:1/4 macromolecular charge ratio (i.e., excess pNS). (C) Histogram of raw intensities of all pixels (i.e., both inside and outside of the condensed phase) for the epifluorescent images shown in (A) and (B). The broad distribution in the pNS channel arises from the dilute/dense intensity variation caused by the high partitioning into the droplet, along with the geometrical variation in intensity arising from epifluorescent imaging of a sphere. The narrow distribution in the PLL channel occurs because there is little variation in concentration inside and outside of the droplet.

Partition coefficients of PLL in pNS-dominated phases

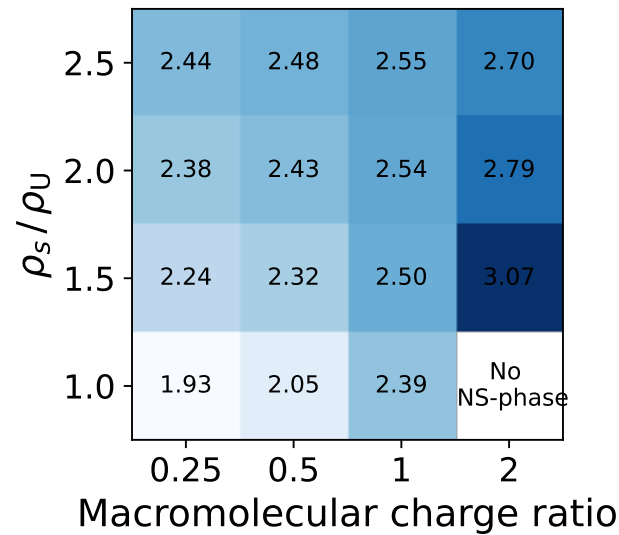


Figure S8. Predicted partition coefficients of PLL in the pNS+PLL systems. The partition coefficients of PLL suggest preferential partitioning into pNS-dominated condensates, even at high salt concentrations.

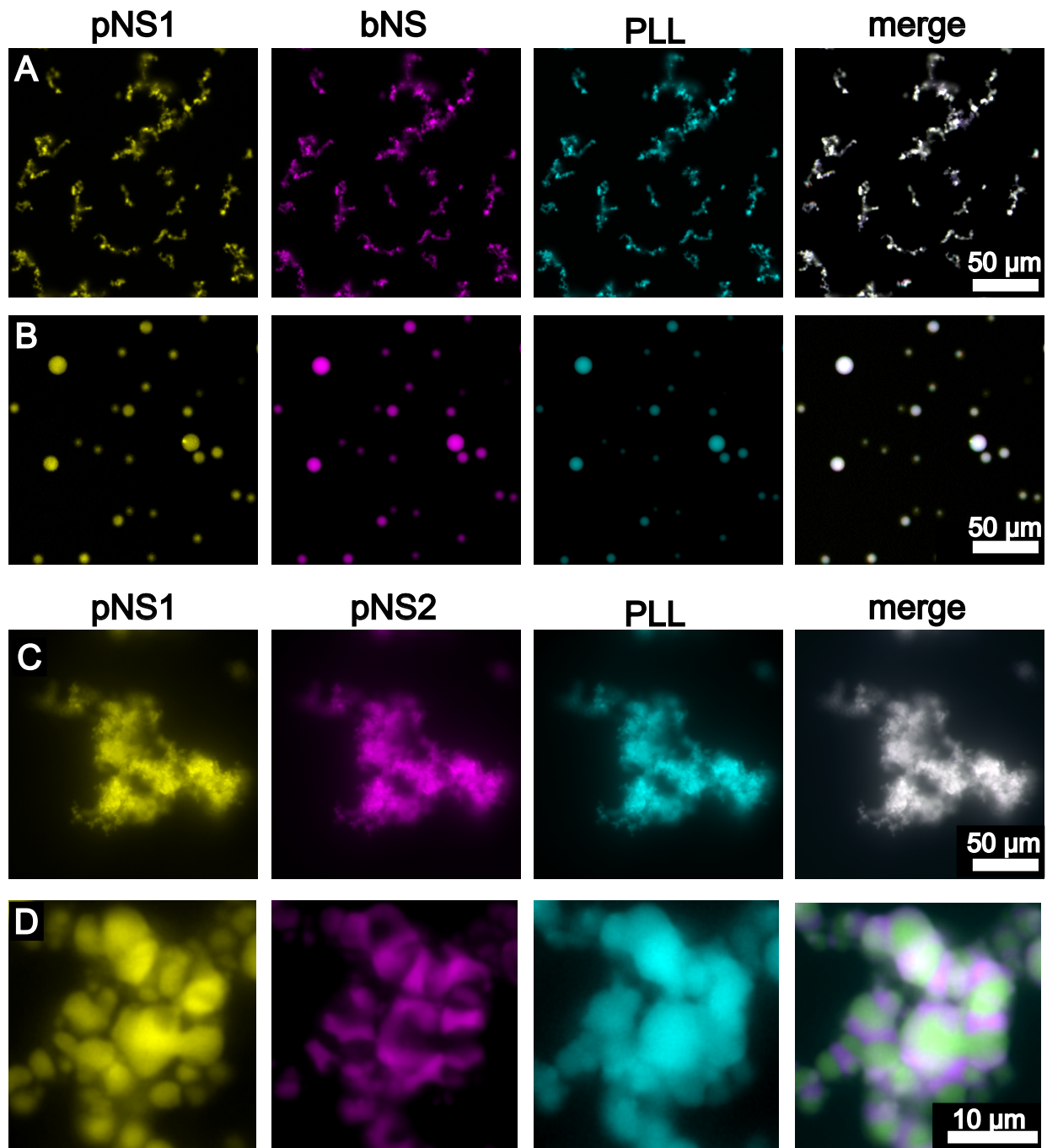


Figure S9. Fluorescent imaging of multiphase structures. PLL (cyan), pNS (yellow) and bNS (magenta) form (A) three-component aggregates at 0.5 M NaCl and (B) three-component liquid drops at 1 M NaCl. (C) Similarly, orthogonal pNS₁ (yellow) and pNS₂ (magenta), along with PLL (cyan), form three-component aggregates at 0.5 M NaCl. (D) However, at 1 M NaCl, the pNS₁+PLL phase demixes from the pNS₂+PLL phase.

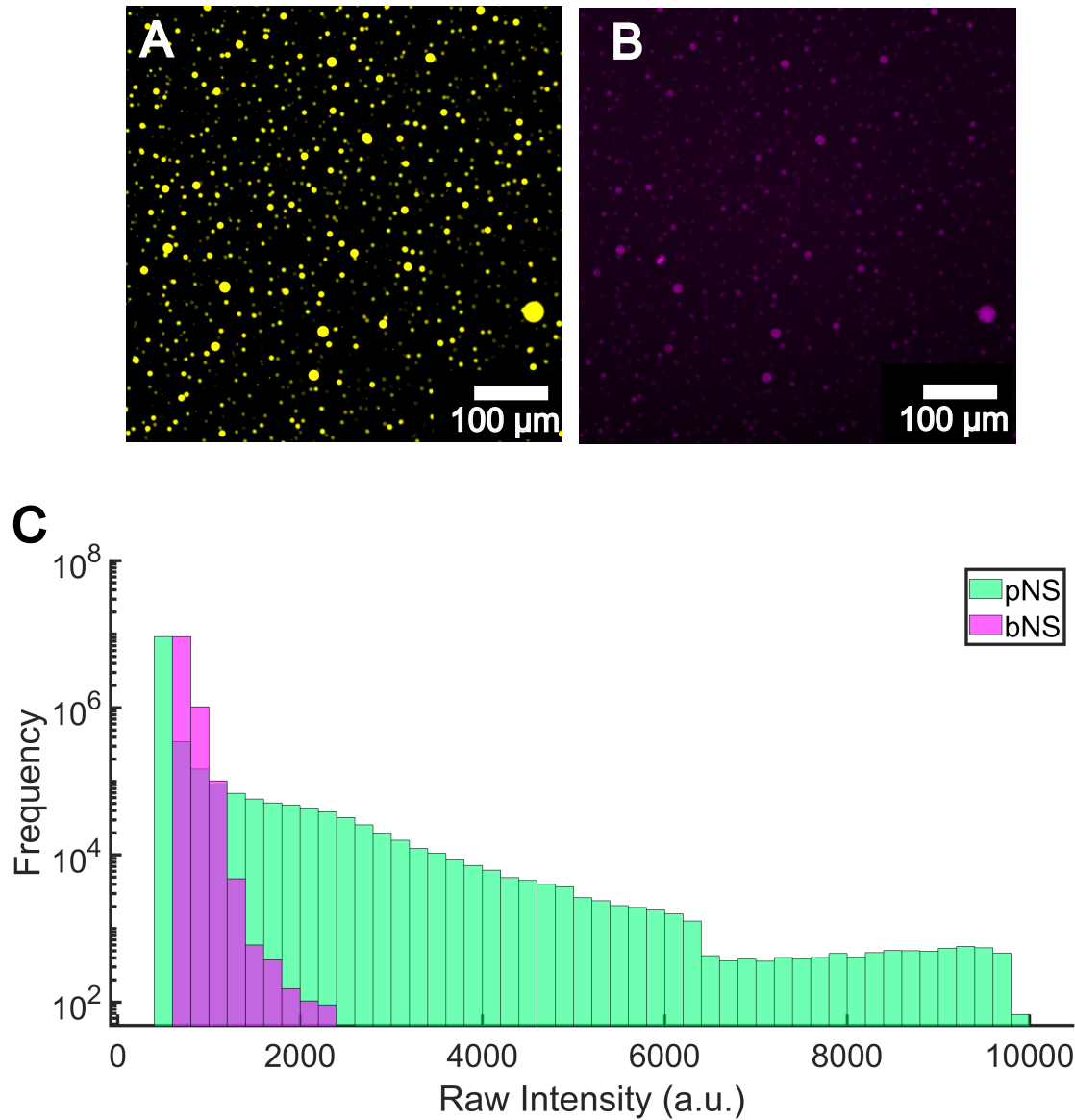


Figure S10. Fluorescent images of droplets in a 3-component solution containing 5 μ M pNS, 5 μ M bNS, and 19.2 μ M PLL, at 1 M NaCl. The images show (A) the pNS channel (yellow), and (B) the bNS channel (magenta). The pixel intensities of (A) and (B) use the same scale to show that pNSs are preferentially enriched relative to bNS in multicomponent droplets. (C) Raw pixel intensities, from three independently prepared replicates, of pNS and bNS channels show a relatively constant bNS signal due to little difference in dense/dilute concentrations, and a wide variation in pNS signal due to the high partitioning.

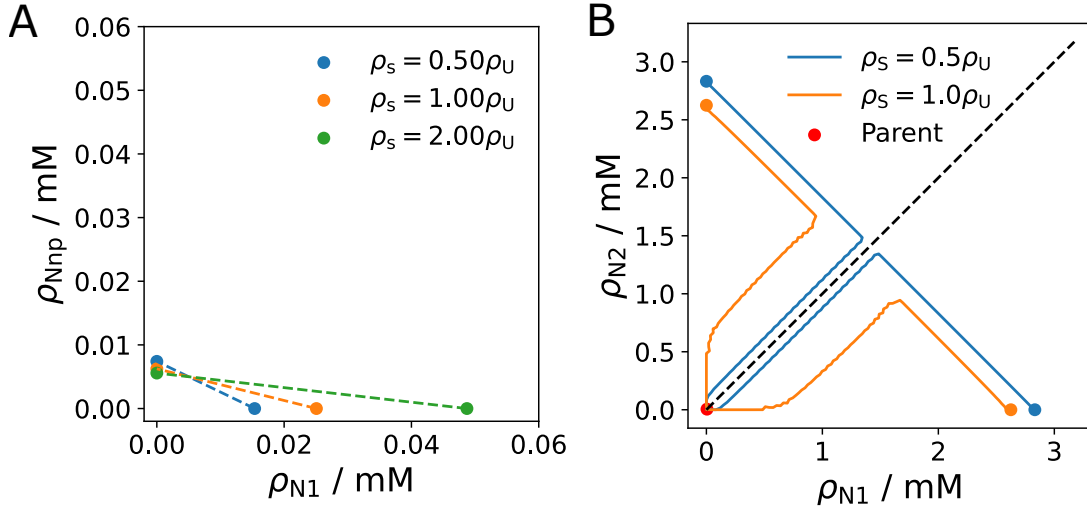


Figure S11. Theoretical predictions for multi-NS systems. (A) The predicted tie lines for systems containing equal amounts of pNS and npNS (parent concentration $\rho_{N1} = \rho_{Nnp} = 5\mu\text{M}$, $\rho_P = 0$) at three salt concentrations. The blunt NS (bNS) is always excluded from the condensed phase regardless of the salt concentration, which differs qualitatively from the behavior shown in Fig. 4C in the main text. (B) Minimum-free-energy path predictions for pNS₁+pNS₂+PLL systems (parent concentration $\rho_{N1} = \rho_{N2} = 5\mu\text{M}$, $\rho_P = 19.2\mu\text{M}$) at two salt concentrations. At low salt concentration, the MFEP passes through an intermediate state enriched in both NS species, where the system may become kinetically trapped. At high salt concentration, distinct phases, each enriched in one or the other pNS species, form almost instantaneously.

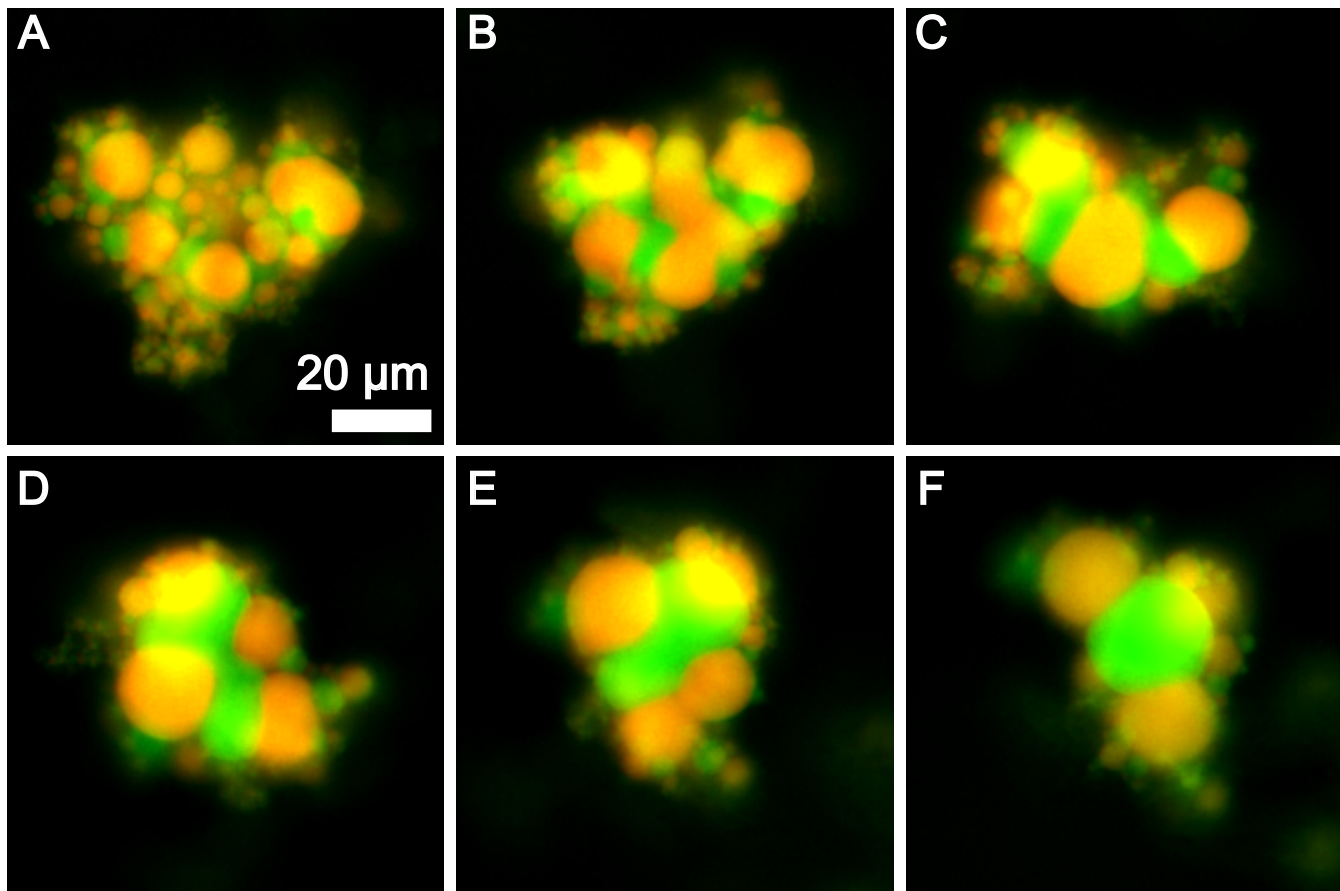


Figure S12. Time series of fluorescent images of droplets formed in a mixture, at 1 M NaCl, of PLL (19.2 μ M, green) with orthogonal pNS₁ (5 μ M, red) and pNS₂ (5 μ M, unlabeled), showing multi-phase clusters that coarsen over time. With this labeling scheme, the droplets enriched in PLL+pNS₁ appear orange, while the droplets enriched in PLL+pNS₂ appear green. Time points are (A) 0 min, (B) 15 min, (C) 30 min, (D) 45 min (E) 60 min, and (F) 165 min after mixing.

S1. OVERVIEW OF THE THEORETICAL MODEL

In our model, NS and PLL polyions are represented at a coarse-grained level by polymer ‘‘blobs’’. Each NS is represented as a single blob, whereas each PLL molecule is represented as a freely jointed chain of $N_p = 10$ Kuhn-length blobs [38]. Each blob carries a Gaussian charge distribution,

$$q_i(r) = Z_i e \left(\frac{1}{2\pi\sigma_i^2} \right)^{\frac{3}{2}} \exp(-r^2/2\sigma_i^2), \quad (\text{S1})$$

where we use the subscript i to indicate NS (N) and PLL (P) species (Figure S13). A blob of species i carries a total charge of $Z_i e$ that is spatially distributed according to the blob radius σ_i . By contrast, microcations (+) and microanions (−) are treated as point particles. We do not distinguish between the different sources of microions, which include both counterions and added monovalent salt, in this model. The implicit solvent is treated as a continuum with relative permittivity ϵ . The number densities of these four ion species, ρ_N , ρ_P , ρ_+ , and ρ_- , are constrained by the electroneutrality condition

$$Z_N \rho_N + N_P Z_P \rho_P + \rho_+ - \rho_- = 0. \quad (\text{S2})$$

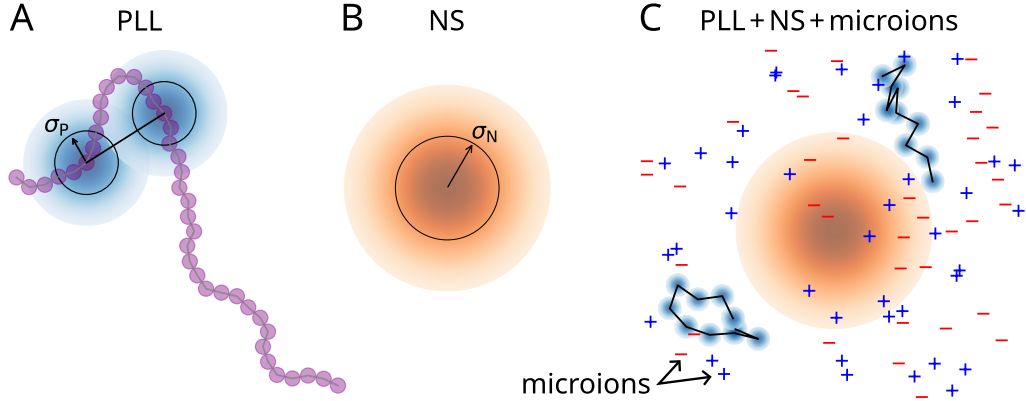


Figure S13. Schematics of (A) a PLL polymer (purple monomers) coarse-grained into Gaussian charge blobs with radii σ_P (blue blobs), (B) a DNA nanostar coarse-grained into a Gaussian charge blob with radius σ_N (orange blob), and (C) the full system, comprising coarse-grained PLL polymers, coarse-grained nanostars, and positively and negatively charged point-particle microions.

The full Hamiltonian of the system includes a polyion contribution H_p that depends only on the polyion blob positions, $\{\mathbf{R}_i\}$; a microion contribution H_m that depends only on the microion positions, $\{\mathbf{r}_i\}$; and a polyion–microion coupling contribution H_{mp} ,

$$H = H_p(\{\mathbf{R}_i\}) + H_m(\{\mathbf{r}_i\}) + H_{mp}(\{\mathbf{R}_i\}, \{\mathbf{r}_j\}). \quad (\text{S3})$$

In what follows, we derive an effective Hamiltonian that depends only on the polyion blob positions,

$$H_{\text{eff}}(\{\mathbf{R}_i\}) = H_p(\{\mathbf{R}_i\}) + F_m(\{\mathbf{R}_i\}). \quad (\text{S4})$$

The polyion Hamiltonian $H_p(\{\mathbf{R}_i\})$ consists of several parts, including the kinetic energy, K_p ; the excluded volume potential, U_{ev} ; the association potential, U_{assoc} ; and the unscreened Coulombic potential due to polyion–polyion interactions, U_C ,

$$H_p = K_p + U_{\text{ev}} + U_{\text{assoc}} + U_C. \quad (\text{S5})$$

The microion-related free energy $F_m(\{\mathbf{R}_i\})$ must be obtained by integrating out the microion positions, $\{\mathbf{r}_i\}$, given fixed polyion positions, $\{\mathbf{R}_i\}$.

To proceed, we first evaluate the unscreened polyion Coulombic potential U_C using the convolution theorem and Parseval's relation,

$$\begin{aligned}
U_C &= \sum_{i < j}^N \int d\mathbf{s} \int d\mathbf{s}' q_i(\mathbf{s} - \mathbf{R}_i) q_j(\mathbf{s}' - \mathbf{R}_j) \frac{1}{\epsilon |\mathbf{s} - \mathbf{s}'|} \\
&= \frac{1}{(2\pi)^3} \sum_{i < j}^N \int d\mathbf{k} q_{i,\mathbf{k}} q_{j,\mathbf{k}} \frac{4\pi}{\epsilon k^2} \exp[i\mathbf{k} \cdot (\mathbf{R}_i - \mathbf{R}_j)] \\
&= \sum_{i < j}^N \frac{Z_i Z_j e^2}{\epsilon |\mathbf{R}_i - \mathbf{R}_j|} \operatorname{erf}\left(\frac{|\mathbf{R}_i - \mathbf{R}_j|}{2\sigma_{ij}}\right), \tag{S6}
\end{aligned}$$

where $\sigma_{ij} \equiv \sqrt{(\sigma_i^2 + \sigma_j^2)/2}$. We then obtain the microion-related free energy, F_m , by minimizing a free energy functional based on Classical Density Functional Theory (CDFT) [28, 47],

$$F_m(\{\mathbf{R}_i\}) = \min \mathcal{F}[\rho_+(\mathbf{r}), \rho_-(\mathbf{r})], \tag{S7}$$

where $\rho_+(\mathbf{r})$ and $\rho_-(\mathbf{r})$ are fields representing the concentrations of positive and negative microions, respectively (Figure S14). See SI Sec. S4 for details of this calculation. The microion-related free energy includes a state-dependent “volume term”, Φ , and pairwise screened electrostatic potentials between polyion blobs, u_{ij}^{eff} ,

$$F_m(\{\mathbf{R}_i\}) = \Phi + \sum_{i < j}^N u_{ij}^{\text{eff}}(R_{ij}) - U_C, \tag{S8}$$

where $R_{ij} \equiv |\mathbf{R}_j - \mathbf{R}_i|$. The volume term, which does not depend on the positions of the polyions, takes the form

$$\begin{aligned}
\Phi &= F_{\text{id}}(V, T, \rho_+) + F_{\text{id}}(V, T, \rho_-) + F_{\text{ev}}(V, T, \rho_N, \rho_P, \rho_+, \rho_-) \\
&\quad - \rho_N V \frac{Z_N^2 e^2 \kappa}{2\epsilon} \exp(\kappa^2 \sigma_N^2) \operatorname{erfc}(\kappa \sigma_N) - N_P \rho_P V \frac{Z_P^2 e^2 \kappa}{2\epsilon} \exp(\kappa^2 \sigma_P^2) \operatorname{erfc}(\kappa \sigma_P) \\
&\quad - \frac{V k_B T}{2(\rho_+ + \rho_-)} (Z_N \rho_N + N_P Z_P \rho_P)^2, \tag{S9}
\end{aligned}$$

where F_{id} is the ideal free energy of a gas at constant volume V , temperature T , and mean concentration ρ_{\pm} , and F_{ev} is the contribution to the free energy due to excluded volume interactions between microions and polyions. The inverse Debye screening length κ is defined as

$$\kappa \equiv [4\pi l_B(\rho_+ + \rho_-)]^{1/2}, \tag{S10}$$

where l_B is the Bjerrum length, $l_B \equiv e^2/\epsilon k_B T$. The screened electrostatic potential between the polyion blobs i and j is

$$\begin{aligned}
u_{ij}^{\text{eff}}(R_{ij}) &= \frac{Z_i Z_j e^2}{\epsilon R_{ij}} \frac{\exp(\kappa^2 \sigma_{ij}^2)}{2} [\exp(-\kappa R_{ij}) \operatorname{erfc}(\kappa \sigma_{ij} - R_{ij}/2\sigma_{ij}) \\
&\quad - \exp(\kappa R_{ij}) \operatorname{erfc}(\kappa \sigma_{ij} + R_{ij}/2\sigma_{ij})]. \tag{S11}
\end{aligned}$$

In these expressions, the complementary error function is defined as

$$\operatorname{erfc}(z) = \frac{2}{\sqrt{\pi}} \int_z^\infty e^{-t^2} dt. \tag{S12}$$

At large distances between polyion blobs, the screened electrostatic potential in Eq. (S11) has the asymptotic formula

$$u_{ij}^{\text{eff}}(R_{ij}) \sim \frac{Z_i Z_j e^2}{\epsilon} \exp(\kappa^2 \sigma_{ij}^2) \frac{\exp(-\kappa R_{ij})}{R_{ij}} \tag{S13}$$

as $R_{ij} \rightarrow \infty$. We notice that Eq. (S13) has the same form as the well known DLVO potential [39, 40], but with a different prefactor. In fact, the DLVO potential can be derived in a similar way from CDFT, in which case the

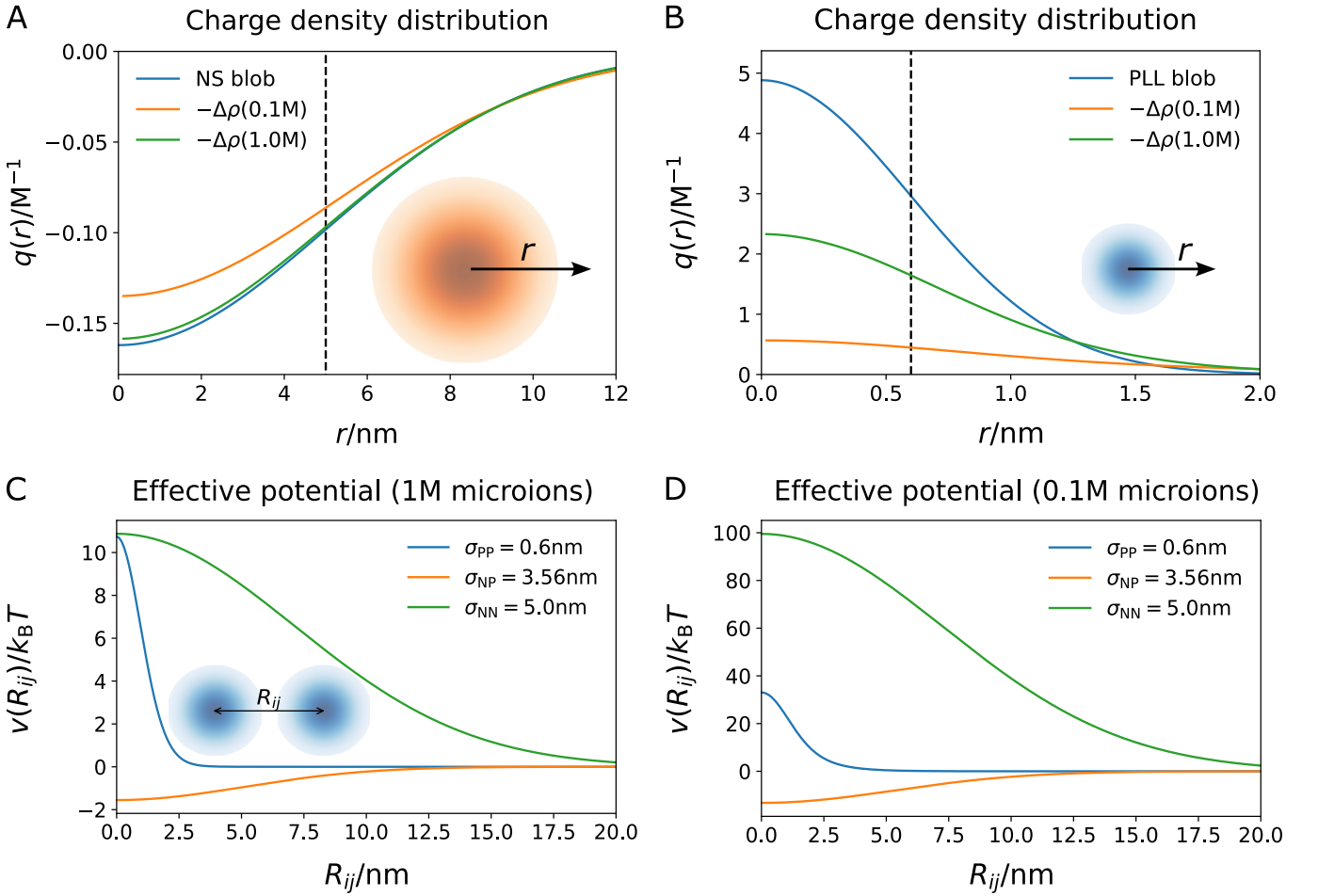


Figure S14. Polyion charge distributions, microion charge density distributions, and the resulting screened electrostatic potentials predicted by CDFT. (A) The polyion charge distribution for a NS blob and the predicted charge density distribution, $\Delta\rho(r) \equiv \rho_+(r) - \rho_-(r)$, of the surrounding microions at 0.1 M and 1 M salt concentrations. The vertical dashed line represents the NS radius, σ_N . (B) The polyion charge distribution for a PLL blob and the predicted charge density distribution of the surrounding microions at 0.1 M and 1 M salt concentrations. The microion distributions are obtained through the Fourier transform of Eq. (S40). The vertical dashed line represents the PLL blob radius, σ_P . (C) The effective potentials between polyion blobs at 1 M salt concentration as a function of the center-to-center distance, R_{ij} , given by Eq. (S11). (D) The effective potentials between polyion blobs at 0.1 M salt concentration.

polyions are represented by hard-sphere colloidal particles with charges uniformly distributed on the surface [47]. The different prefactor reflects the influence of the continuous charge distribution that we assume for each polyion blob.

Finally, we evaluate the free-energy density (i.e., the free energy per unit volume) of the full system, f , using the effective Hamiltonian $H_{\text{eff}}(\{\mathbf{R}_i\})$. We approximate the contribution to f due to the pairwise polyion–polyion screened electrostatic potential using the mean-field expression

$$\begin{aligned} f_{\text{mf}} &= 2\pi \sum_{i,j} \rho_i \rho_j \int_0^\infty dR_{ij} u_{ij}^{\text{eff}}(R_{ij}) R_{ij}^2 \\ &= \frac{k_B T}{2(\rho_+ + \rho_-)} (Z_N \rho_N + N_P Z_P \rho_P)^2. \end{aligned} \quad (\text{S14})$$

This expression exactly cancels the last contribution to the volume term, Eq. (S9). Moreover, because the unscreened Coulombic potential in H_p , Eq. (S5), is canceled by F_m , Eq. (S8), the only surviving contributions due to electrostatics are contained in the “self-energy” terms in Eq. (S9),

$$f_{\text{self}} = -\frac{k_B T \kappa l_B}{2} [\rho_N Z_N^2 \exp(\kappa^2 \sigma_N^2) \operatorname{erfc}(\kappa \sigma_N) + N_P \rho_P Z_P^2 \exp(\kappa^2 \sigma_P^2) \operatorname{erfc}(\kappa \sigma_P)]. \quad (\text{S15})$$

The other, non-electrostatic contributions to f arise from the remaining terms in Eq. (S5) and Eq. (S9). Taken together, we write the complete mean-field free-energy density of the system as

$$f = f_{\text{poly}} + f_{\text{micro}} + f_{\text{self}} + f_{\text{assoc}}, \quad (\text{S16})$$

where f_{poly} accounts for the polyion ideal free energy and the polyion excluded volume potential U_{ev} in Eq. (S5), f_{micro} accounts for the microion ideal free energy and the excluded volume interactions between microions and polyions in Eq. (S9), and f_{assoc} accounts for the association potential between NS sticky ends in Eq. (S5). Expressions for these terms, which are evaluated using a previously developed extension of the Flory–Huggins theory [42], the Widom insertion method [43], and Wertheim’s thermodynamic perturbation theory [41], respectively, are provided in the Methods section of the main text.

S2. PARAMETRIZATION OF THE THEORETICAL MODEL

We summarize the model parameters and provide explanations for their values in Table S2.

Parameter	Value	Explanation
σ_N	5 nm	Approximate hydrodynamic radius (~ 4.7 nm [48])
σ_P	0.6 nm	Comparable to the persistence length (~ 1 nm [38])
N_P	10	The number of Kuhn segments assuming ~ 10 lysine monomers per Kuhn segment [38]
Z_N	-192	The total charge per NS
Z_P	10	The total charge per PLL Kuhn segment
l_B	0.71 nm	Bjerrum length for pure water at 25°C
f_N	0.01	NS blobs are mostly solvent, with DNA occupying a relatively small volume fraction.
f_P	0.5	Roughly half of the volume of each PLL blob is sterically inaccessible to microions.

Table S2. The physics-based and system-specific constants used to parametrize the theoretical model.

To parametrize the association contribution to the mean-field free-energy density, f_{assoc} , we compute the dimensionless association strength due to sticky-end base pairing, Δ . This parameter is utilized in Wertheim’s thermodynamic perturbation theory, as described in the Methods section of the main text. At a standard 1 M monovalent cation concentration in aqueous solution, this parameter is

$$\Delta_0 = \frac{m\Omega}{4\pi} \exp(-\beta\Delta G^\circ) v_N^{-1} \cdot M^{-1}, \quad (\text{S17})$$

where $m = 4$ is the number of sticky ends per pNS, Ω is the solid angle accessible to a sticky end on a pNS blob, and $v_N = 4\pi\sigma_N^3/3$ is the pervaded volume of a NS. The sequence and temperature-dependent hybridization free energy ΔG° is calculated using NUPACK [45]. We then apply an empirical salt correction [23]

$$\Delta = \Delta_0 (\rho_+ \cdot M^{-1})^\alpha, \quad (\text{S18})$$

where $\alpha = 1.15$, to obtain the dimensionless association strength Δ at nonstandard salt concentrations. This correction accounts for the effective strengthening of DNA hybridization due to screening of the charges on the DNA sticky ends by added salt.

We note that the standard hybridization free energy, ΔG° , already includes the effects of screened electrostatics involving the DNA sticky ends at 1 M salt. However, our theory also considers these charges in the electrostatic contributions to our mean-field theory, since the sticky-end charges are included in Z_N . We therefore strengthen the standard hybridization free energy relative to the NUPACK prediction to avoid double counting. By comparing the predicted free-energy landscapes of a pNS-only solution with and without explicit charges on the sticky ends (i.e., with $Z_N = -192$, and with $Z_N = -192 + 4 \times 7 = -164$, respectively) at 1 M salt, we determine that the NUPACK-predicted value of ΔG° should be decreased by $3.06k_B T$ in the presence of explicit charges (Figure S15A). Finally, we estimate that the solid angle accessible to an individual sticky end on a pNS is approximately $\Omega = \pi/4$ based on our previous work [44]. Applying this parametrization approach to the experimental palindromic sticky-end sequence (including the first non-hybridizing base), 5'-CGATCGA-3', results in the temperature-dependent Δ_0 values shown in Figure S15B.

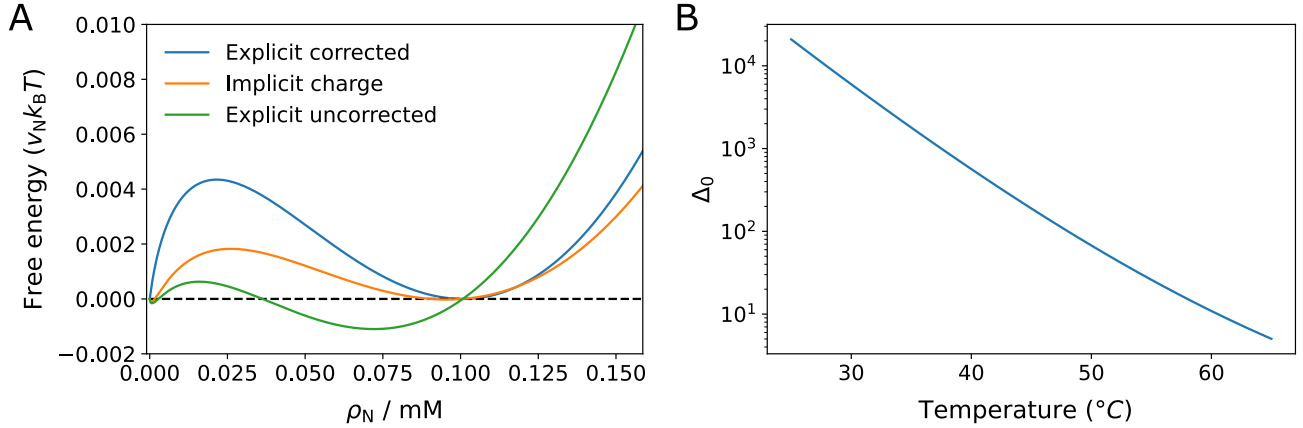


Figure S15. Parameterization of the dimensionless association strength due to sticky-end base pairing at 1 M NaCl, Δ_0 . (A) Comparison of predicted pNS-only free-energy landscapes with explicit charges (i.e., with the physical value of Z_N given in Table S2) and implicit charges on the sticky ends (i.e., with $Z_N = -192 + 4 \times 7 = -164$) at 25 °C. Explicit-charge landscapes are shown both with the corrected ΔG° value (blue curve) and with the NUPACK-predicted ΔG° value (green curve). The implicit-charge landscape is computed with the NUPACK-predicted ΔG° value (orange curve). The correction to ΔG° is chosen such that the explicit-charge and implicit-charge landscapes predict the same coexistence pNS concentrations; the blue and orange curves have been shifted by a linear term per the common-tangent construction, so that the coexisting phases coincide with local minima on these curves. (B) Δ_0 as a function of temperature.

S3. PHASE-COEXISTENCE AND MINIMUM-FREE-ENERGY-PATH CALCULATIONS

Using the free-energy density f , we calculate the conditions for phase coexistence following the numerical strategy described in our previous work [49]. We reproduce the details of this numerical approach here for completeness. Specifically, we solve for the molecular number densities, $\{\vec{\rho}^{(k)}\}$, and the mole fractions of the coexisting phases, $\{x^{(k)}\}$, given the total molecular number densities, $\vec{\rho}_{\text{tot}}$. Mass conservation requires that

$$\vec{\rho}_{\text{tot}} = \sum_{k=1}^K x^{(k)} \vec{\rho}^{(k)}, \quad (\text{S19})$$

if there are K phases in coexistence.

We now consider the conditions for phase equilibrium in a mixture with $N = 3$ independent components (NS, PLL, and microcations), since the microanion concentration is constrained by the charge neutrality condition in Eq. (S2). The grand-potential density is related to the free-energy density via $\omega = f - \sum_{i=1}^N (\partial f / \partial \rho_i) \rho_i$, where the chemical potentials of the non-solvent molecular species are $\mu_i = \partial f / \partial \rho_i$. Coexisting phases are located at minima of ω , ensuring that all components have equal chemical potentials in all phases. Phase equilibrium also requires equal pressures across all coexisting phases, implying that the $\omega(\vec{\rho})$ has the same value at all local minima. Together, these conditions require

$$\omega(\vec{\rho}^{(k)}) = \min \omega(\vec{\rho}; \vec{\mu}). \quad (\text{S20})$$

We solve Eq. (S20) numerically by minimizing the norm of the residual errors of Eq. (S19) and Eq. (S20) iteratively. At each iteration, we first locate the local minima of the grand potential, $\vec{\rho}^{(k)} = \arg \min_{\vec{\rho}} \omega(\vec{\rho}; \vec{\mu})$ for all phases $k = 1, \dots, K$, using the Nelder–Mead method [50]. We then update $\vec{\mu}$ and $\{x^{(k)}\}$ using the modified Powell method [51].

Success of this optimization procedure requires that the initial estimates of $\{\vec{\rho}^{(k)}\}$ are not too far from the values at coexistence. We obtain an initial guess for $\{\vec{\rho}^{(k)}\}$ from the convex hull method [49, 52], in which we compute the convex hull of points on a discretized $(N + 1)$ -dimensional free energy surface. We initialize our optimization procedure with $N + 1$ vectors $\{\vec{\rho}^{(k)}\}$ that correspond to the vertices of the convex hull facet that encompasses $\vec{\rho}_{\text{tot}}$. From the linear equation that defines this facet, we also obtain initial guesses for $\vec{\mu}$ and $\{x^{(k)}\}$. When the number of coexisting phases K is less than $N + 1$, some of the $N + 1$ vectors $\{\vec{\rho}^{(k)}\}$ are identical to within numerical tolerance after optimization; in this case, we restart the optimization procedure with a unique set of vectors and the corresponding $\vec{\mu}$ and $\{x^{(k)}\}$. In this way, we determine the number of coexisting phases, K , as well as the molecular number-density vectors, $\{\vec{\rho}^{(k)}\}$, and chemical potentials, $\vec{\mu}$, at phase coexistence.

To investigate the system's phase-separation kinetics, we examine the grand potential at fixed chemical potentials corresponding to a homogeneous system with the total number densities $\vec{\rho}_{\text{tot}}$,

$$\omega_0(\vec{\rho}) = f - \sum_{i=1}^N (\partial f / \partial \rho_i)_{\vec{\rho}_{\text{tot}}} \rho_i. \quad (\text{S21})$$

We then compute the minimum-free-energy path (MFEP) to each of the condensed phases using the zero-temperature string method [46]. Following the terminology in Ref. [46], we use a total of $M = 100$ points on a string between two local minima on the free energy surface. In the “evolution step” of the algorithm, the points evolve according to the gradient descent method:

$$\vec{\rho}_k^{(l+1)} = \vec{\rho}_k^{(l)} - \Delta t \left(\frac{\partial \omega_0}{\partial \vec{\rho}} \right)_{\vec{\rho}_k^{(l)}}, \quad (\text{S22})$$

where the step size takes $\Delta t = 5 \times 10^{-4}$. Then in the “reparametrization step”, we reparametrize the string such that the M points are equally spaced with respect to arc length along the string. We check for convergence by measuring the norm of the displacement of all points from their positions in the previous iteration, and we use a convergence tolerance of $\text{TOL} = 5 \times 10^{-6}$.

S4. DERIVATION OF THE MICROION-RELATED FREE ENERGY USING CDFT

In this section, we derive the microion-related free energy, $F_m(\{\mathbf{R}_i\})$, by extending the classical density functional theory (CDFT) derivation in Ref. [28] to multicomponent polyion systems. We write the free energy functional as

$$\mathcal{F}[\rho_+(\mathbf{r}), \rho_-(\mathbf{r})] = \mathcal{F}_{\text{id}} + \mathcal{F}_m + \mathcal{F}_{\text{pm}}, \quad (\text{S23})$$

where $\rho_{\pm}(\mathbf{r}) \equiv \rho_{\pm}^{(1)}(\mathbf{r})$ is the number density [53] of microions with charge $+1$ or -1 , respectively, and we neglect microion correlations. We consider local microion inhomogeneities,

$$\Delta \rho_{\pm}(\mathbf{r}) \equiv \rho_{\pm}(\mathbf{r}) - \rho_{\pm}, \quad (\text{S24})$$

where $\rho_{\pm} = V^{-1} \int d\mathbf{r} \rho_{\pm}(\mathbf{r})$ is the mean number density of each microion species. This allows us to expand the ideal gas part of the free-energy functional to quadratic order,

$$\mathcal{F}_{\text{id}} = \sum_{\alpha=\pm} \left[F_{\text{id}}(V, T, \rho_{\alpha}) + \frac{k_{\text{B}} T}{2\rho_{\alpha}} \int d\mathbf{s} (\Delta \rho_{\alpha}(\mathbf{s}))^2 \right], \quad (\text{S25})$$

where $F_{\text{id}}(V, T, \rho_{\alpha}) = V k_{\text{B}} T \rho_{\alpha} [\ln(\rho_{\alpha} \Lambda_{\alpha}^3) - 1]$ is the homogeneous ideal gas contribution from microion species $\alpha = \pm$. The microion–microion Coulomb interactions contribute to the free-energy functional in the Hartree form,

$$\mathcal{F}_m = \frac{e^2}{2\epsilon} \int d\mathbf{s} \int d\mathbf{s}' \frac{[\rho_+(\mathbf{s}) - \rho_-(\mathbf{s})][\rho_+(\mathbf{s}') - \rho_-(\mathbf{s}')]}{|\mathbf{s} - \mathbf{s}'|}. \quad (\text{S26})$$

Meanwhile, the microion–polyion contribution takes the form

$$\mathcal{F}_{\text{pm}} = \sum_{\alpha=\pm} \int d\mathbf{s} \rho_{\alpha}(\mathbf{s}) U_{\alpha}(\mathbf{s}) - (\rho_+ + \rho_-) \ln(1 - \eta), \quad (\text{S27})$$

where the potential experienced by the microions due to the N polyions with Gaussian charge distributions, Eq. (S1), is

$$U_+(\mathbf{r}) = -U_-(\mathbf{r}) = \sum_{i=1}^N Z_i \frac{e^2}{\epsilon |\mathbf{r} - \mathbf{R}_i|} \text{erf} \left(\frac{|\mathbf{r} - \mathbf{R}_i|}{\sqrt{2}\sigma_i} \right). \quad (\text{S28})$$

The final term in the expression for \mathcal{F}_{pm} describes the polyion–microion excluded volume contribution to the free energy, where η is the volume fraction of the system that is sterically inaccessible to microions. As discussed in the Methods section of the main text, this term is derived using the Widom insertion method [43] assuming that the volume occupied by each microion is negligible.

We diagonalize \mathcal{F} by defining

$$\rho(\mathbf{r}) \equiv \rho_+(\mathbf{r}) - \rho_-(\mathbf{r}) \quad (\text{S29})$$

and

$$\delta(\mathbf{r}) \equiv \frac{\rho_-\rho_+(\mathbf{r}) + \rho_+\rho_-(\mathbf{r})}{\rho_+ + \rho_-}. \quad (\text{S30})$$

The functional can then be written as

$$\mathcal{F}[\rho, \delta] = F_{\text{id}}(V, T, \rho_+) + F_{\text{id}}(V, T, \rho_-) - (\rho_+ + \rho_-) \ln(1 - \eta) + \mathcal{F}_1[\rho] + \mathcal{F}_2[\delta], \quad (\text{S31})$$

where

$$\mathcal{F}_1[\rho] = \frac{k_{\text{B}}T}{2(\rho_+ + \rho_-)} \int d\mathbf{s} [\rho(\mathbf{s}) - \bar{\rho}]^2 + \int d\mathbf{s} \rho(\mathbf{s}) U(\mathbf{s}) + \frac{e^2}{2\epsilon} \int d\mathbf{s} \int d\mathbf{s}' \frac{\rho(\mathbf{s})\rho(\mathbf{s}')}{|\mathbf{s} - \mathbf{s}'|}, \quad (\text{S32})$$

$$\mathcal{F}_2[\delta] = \frac{k_{\text{B}}T}{2} \left(\frac{1}{\rho_+} + \frac{1}{\rho_-} \right) \int d\mathbf{s} [\delta(\mathbf{s}) - \bar{\delta}]^2 + \int d\mathbf{s} \delta(\mathbf{s}) W(\mathbf{s}), \quad (\text{S33})$$

and $\bar{\rho}$ and $\bar{\delta}$ are the spatial averages of the variational fields, $\bar{\rho} \equiv \rho_+ - \rho_-$ and $\bar{\delta} \equiv 2\rho_+\rho_-/(\rho_+ + \rho_-)$. The definitions of the muticentered functions $U(\mathbf{r})$ and $W(\mathbf{r})$ follow from the linear combinations of the external fields,

$$U(\mathbf{r}) = \frac{\rho_+ U_+(\mathbf{r}) - \rho_- U_-(\mathbf{r})}{\rho_+ + \rho_-} \quad (\text{S34})$$

and

$$W(\mathbf{r}) = U_+(\mathbf{r}) + U_-(\mathbf{r}). \quad (\text{S35})$$

Due to the \pm symmetry of Eq. (S28), we find that $U(\mathbf{r}) = U_+(\mathbf{r})$ and $W(\mathbf{r}) = 0$. The functional $\mathcal{F}_2[\delta]$ is therefore minimized by setting $\delta(\mathbf{r}) = \bar{\delta}$, indicating that this contribution to \mathcal{F} vanishes at equilibrium.

To minimize $\mathcal{F}_1[\rho]$, we solve the Euler–Lagrange (EL) equation

$$\mu_{\rho} = \frac{\partial \mathcal{F}_1[\rho]}{\partial \rho(\mathbf{r})} = \frac{k_{\text{B}}T}{n} \Delta \rho(\mathbf{r}) + U(\mathbf{r}) + \frac{e^2}{\epsilon} \int d\mathbf{s}' \frac{\rho(\mathbf{s}')}{|\mathbf{r} - \mathbf{s}'|}, \quad (\text{S36})$$

where $n \equiv \rho_+ + \rho_-$ and $\Delta \rho(\mathbf{r}) \equiv \rho(\mathbf{r}) - \bar{\rho}$. To handle divergences in the volume integrals, we employ a screened Coulomb potential, i.e., $\exp(-\lambda r)r^{-1}$, in place of r^{-1} and take the limit $\lambda \rightarrow 0$ later. We denote the screened form of U by $U^{(\lambda)}$ in what follows. Using the Fourier transform

$$f_{\mathbf{k}} = \int_V d\mathbf{s} f(\mathbf{s}) \exp(i\mathbf{k} \cdot \mathbf{s}), \quad (\text{S37})$$

we obtain

$$\mu_{\rho} (2\pi)^3 \delta(\mathbf{k}) = \frac{k_{\text{B}}T}{n} \Delta \rho_{\mathbf{k}} + U_{\mathbf{k}}^{(\lambda)} + \frac{e^2}{\epsilon} \frac{4\pi}{k^2 + \lambda^2} [(2\pi)^3 \bar{\rho} \delta(\mathbf{k}) + \Delta \rho_{\mathbf{k}}]. \quad (\text{S38})$$

Then, using $(2\pi)^3 \delta(\mathbf{k} = 0) = V$ and $\Delta \rho_{\mathbf{k}=0} = 0$, we can write the $\mathbf{k} = 0$ component as

$$\mu_{\rho} V = U_{\mathbf{k}=0}^{(\lambda)} + \frac{4\pi e^2}{\epsilon \lambda^2} \bar{\rho} V. \quad (\text{S39})$$

The explicit solution to the EL equation now reads

$$k_{\text{B}}T \Delta \rho_{\mathbf{k}} = -n \frac{k^2 + \lambda^2}{k^2 + \kappa_{\lambda}^2} U_{\mathbf{k}}^{(\lambda)} + \frac{(2\pi)^3 \delta(\mathbf{k})}{V} n \frac{\lambda^2}{\kappa_{\lambda}^2} U_{\mathbf{k}=0}^{(\lambda)}, \quad (\text{S40})$$

where we have introduced the inverse Debye screening length, κ , and its modified counterpart κ_{λ} . These quantities are given by

$$\kappa^2 \equiv \frac{4\pi e^2 (\rho_+ + \rho_-)}{\epsilon k_{\text{B}}T} = 4\pi l_{\text{B}} (\rho_+ + \rho_-) \quad (\text{S41})$$

and $\kappa_\lambda^2 \equiv \kappa^2 + \lambda^2$, where l_B is the Bjerrum length. Example plots of $\Delta\rho(r)$, obtained from the inverse Fourier transform of Eq. (S40) with $\lambda \rightarrow 0$, are shown in Figure S14A,B.

We now evaluate \mathcal{F}_1 at its minimum, using Eq. (S40), to obtain the equilibrium free energy F_1 . In its Fourier representation, F_1 is

$$F_1 = -\frac{\rho_+ + \rho_-}{2k_B T} \frac{1}{(2\pi)^3} \int d\mathbf{k} \frac{k^2 + \lambda^2}{k^2 + \kappa_\lambda^2} U_{-\mathbf{k}}^{(\lambda)} U_{\mathbf{k}}^{(\lambda)} + \frac{\rho_+ + \rho_-}{2V k_B T} \frac{\lambda^2}{\kappa_\lambda^2} (U_{\mathbf{k}=0}^{(\lambda)})^2 + \bar{\rho} U_{\mathbf{k}=0}^{(\lambda)} + \frac{2\pi e^2}{\epsilon \lambda^2} \bar{\rho}^2 V. \quad (\text{S42})$$

The first term in Eq. (S42) can be evaluated as

$$\begin{aligned} & -\frac{\rho_+ + \rho_-}{2k_B T} \frac{1}{(2\pi)^3} \int d\mathbf{k} \frac{k^2 + \lambda^2}{k^2 + \kappa_\lambda^2} U_{-\mathbf{k}}^{(\lambda)} U_{\mathbf{k}}^{(\lambda)} \\ &= -\frac{\rho_+ + \rho_-}{2k_B T} \frac{1}{(2\pi)^3} \int d\mathbf{k} \frac{k^2 + \lambda^2}{k^2 + \kappa_\lambda^2} \sum_{i=1}^N \sum_{j=1}^N u_{i,-\mathbf{k}}^{(\lambda)} u_{j,\mathbf{k}}^{(\lambda)} \exp(i\mathbf{k} \cdot \mathbf{R}_{ij}) \\ &= -\frac{1}{(2\pi)^3} \frac{2\pi}{\epsilon} \int d\mathbf{k} \left(\frac{1}{k^2} - \frac{1}{k^2 + \kappa^2} \right) \sum_{i=1}^N \sum_{j=1}^N q_{i,\mathbf{k}} q_{j,\mathbf{k}} \exp(i\mathbf{k} \cdot \mathbf{R}_{ij}), \end{aligned} \quad (\text{S43})$$

where we have used the (screened) Coulombic potential due to polyion blob i , $u_{i,\mathbf{k}}^{(\lambda)} = 4\pi q_{i,\mathbf{k}}/\epsilon(k^2 + \lambda^2)$, in accordance with Eq. (S28), and $q_{i,\mathbf{k}}$ is the Fourier transform of the polyion blob charge distribution. The limit $\lambda \rightarrow 0$ is taken in the final line.

We first evaluate the pairwise part of Eq. (S43) for $i \neq j$. The $1/k^2$ terms in Eq. (S43) sum to $-U_C$ and thus cancel the unscreened Coulombic potentials in Eq. (S6). The remaining terms constitute the effective pair potentials between polyion blobs, $\sum_{i \neq j} u_{ij}^{\text{eff}}(R_{ij})$, where

$$\begin{aligned} u_{ij}^{\text{eff}}(R_{ij}) &= \frac{1}{(2\pi)^3} \frac{4\pi}{\epsilon} \int d\mathbf{k} \frac{1}{k^2 + \kappa^2} q_{i,\mathbf{k}} q_{j,\mathbf{k}} \exp(i\mathbf{k} \cdot \mathbf{R}_{ij}) \\ &= \frac{Z_i Z_j e^2 \exp(\kappa^2 \sigma_{ij}^2)}{\epsilon R_{ij}} \frac{1}{2} [\exp(-\kappa R_{ij}) \operatorname{erfc}(\kappa \sigma_{ij} - R_{ij}/2\sigma_{ij}) - \exp(\kappa R_{ij}) \operatorname{erfc}(\kappa \sigma_{ij} + R_{ij}/2\sigma_{ij})]. \end{aligned} \quad (\text{S44})$$

We then evaluate the $i = j$ terms in Eq. (S43), which correspond to the “self energies” due to the interactions between each polyion and its microion cloud. The total self energy for all N polyions is

$$F_{\text{self}} = -\rho_N V \frac{Z_N^2 e^2 \kappa}{2\epsilon} \exp(\kappa^2 \sigma_N^2) \operatorname{erfc}(\kappa \sigma_N) - N_P \rho_P V \frac{Z_P^2 e^2 \kappa}{2\epsilon} \exp(\kappa^2 \sigma_P^2) \operatorname{erfc}(\kappa \sigma_P). \quad (\text{S45})$$

To evaluate the remaining terms in Eq. (S42), we expand $U_{\mathbf{k}=0}^{(\lambda)}$ with respect to λ . We consider each polyion blob i individually,

$$\begin{aligned} u_{i,\mathbf{k}=0}^{(\lambda)} &= 4\pi \frac{Z_i e^2}{\epsilon} \int_0^\infty \operatorname{erf}\left(\frac{s}{\sqrt{2}\sigma_i}\right) e^{-\lambda s} s ds \\ &= 4\pi \frac{Z_i e^2}{\epsilon} \left[\left(\frac{1}{\lambda^2} - \sigma_i^2 \right) \exp\left(\frac{\lambda^2 \sigma_i^2}{2}\right) \operatorname{erfc}\left(\frac{\lambda \sigma_i}{\sqrt{2}}\right) + \sqrt{\frac{2}{\pi}} \frac{\sigma_i}{\lambda} \right] \\ &= 4\pi \frac{Z_i e^2}{\epsilon} \left[\frac{1}{\lambda^2} - \frac{\sigma_i^2}{2} + \mathcal{O}(\lambda) \right], \end{aligned} \quad (\text{S46})$$

and then perform the sum over all polyions to obtain

$$\begin{aligned} U_{\mathbf{k}=0}^{(\lambda)} &= V \left(\rho_P N_P u_{P,\mathbf{k}=0}^{(\lambda)} + \rho_N u_{N,\mathbf{k}=0}^{(\lambda)} \right) \\ &= 4\pi V \frac{e^2}{\epsilon} \left(\frac{-\bar{\rho}}{\lambda^2} - \frac{\rho_P N_P Z_P \sigma_P^2 + \rho_N Z_N \sigma_N^2}{2} \right) + \mathcal{O}(\lambda), \end{aligned} \quad (\text{S47})$$

where we have used the electroneutrality condition

$$\bar{\rho} + \sum_{i=1}^m Z_i n_i = 0 \quad (\text{S48})$$

in the last line. Similarly, we expand the term in Eq. (S42) that includes $(U_{\mathbf{k}=0}^{(\lambda)})^2$ to obtain

$$\begin{aligned} \frac{\rho_+ + \rho_-}{2Vk_B T} \frac{\lambda^2}{\kappa_\lambda^2} (U_{\mathbf{k}=0}^{(\lambda)})^2 &= \frac{1}{2V} \frac{\kappa^2 \epsilon}{4\pi e^2} \frac{\lambda^2}{\kappa^2} \left(1 - \frac{\lambda^2}{\kappa^2}\right) (U_{\mathbf{k}=0}^{(\lambda)})^2 + \mathcal{O}(\lambda) \\ &= 2\pi V \frac{e^2}{\epsilon} \left[\frac{\bar{\rho}^2}{\lambda^2} - \frac{\bar{\rho}^2}{\kappa^2} + \bar{\rho}(\rho_P N_P Z_P \sigma_P^2 + \rho_N Z_N \sigma_N^2) \right] + \mathcal{O}(\lambda). \end{aligned} \quad (\text{S49})$$

The last three terms of Eq. (S42) therefore simplify to

$$\frac{\rho_+ + \rho_-}{2Vk_B T} \frac{\lambda^2}{\kappa_\lambda^2} (U_{\mathbf{k}=0}^{(\lambda)})^2 + \bar{\rho} U_{\mathbf{k}=0}^{(\lambda)} + \frac{2\pi e^2}{\epsilon \lambda^2} \bar{\rho}^2 V = -\frac{V k_B T}{2(\rho_+ + \rho_-)} \bar{\rho}^2. \quad (\text{S50})$$

Combining the results from Eq. (S31), Eq. (S43), Eq. (S44), Eq. (S45), and Eq. (S50), we summarize the minimized free energy functional, which is $F_m(\{\mathbf{R}_i\})$ in Eq. (S4),

$$\begin{aligned} F_m(\{\mathbf{R}_i\}) &= \min \mathcal{F}[\rho_+(\mathbf{r}), \rho_-(\mathbf{r})] \\ &= F_{\text{id}}(V, T, \rho_+) + F_{\text{id}}(V, T, \rho_-) - (\rho_+ + \rho_-) \ln(1 - \eta) \\ &\quad - U_C + \sum_{i < j}^N u_{ij}^{\text{eff}}(R_{ij}) + F_{\text{self}} - \frac{V k_B T}{2(\rho_+ + \rho_-)} \bar{\rho}^2. \end{aligned} \quad (\text{S51})$$

This expression can be rearranged to separate the $\{\mathbf{R}_i\}$ -dependent terms and the remaining “volume” terms, as presented in Eq. (S8) and Eq. (S9).